Compensation for Camera Motion on Unsteady Robots for Optical Flow

Fernando L. Garcia Bermudez

Electrical Engineering and Computer Sciences
University of California at Berkeley

Technical Report No. UCB/EECS-2013-240
http://www.eecs.berkeley.edu/Pubs/TechRpts/2013/EECS-2013-240.html

December 20, 2013

Compensation for Camera Motion on Unsteady Robots for Optical Flow

by

Fernando Luis Garcia Bermudez

A dissertation submitted in partial satisfaction of the
requirements for the degree of
Doctor of Philosophy

in

Engineering – Electrical Engineering and Computer Sciences

in the

Graduate Division

of the

University of California, Berkeley

Committee in charge:

Professor Ronald S. Fearing, Chair
Professor Ruzena Bajcsy
Professor Bruno Olshausen

Fall 2013

Compensation for Camera Motion on Unsteady Robots for Optical Flow

Abstract

Compensation for Camera Motion on Unsteady Robots for Optical Flow

by

Fernando Luis Garcia Bermudez

Doctor of Philosophy in Engineering – Electrical Engineering and Computer Sciences

University of California, Berkeley

Professor Ronald S. Fearing, Chair

Some modes of locomotion, such as legged walking and flapping flight, are inherently unsteady due to the cyclic interaction of the subject's limbs with a changing and largely unmodelled environment. Bio-inspired robots that locomote this way, present a unique challenge to indoor navigation because the sensors used for exteroception record this unsteadiness in their readings. A legged crawler's unsteady dynamics are explored with an emphasis on how these affect optical flow estimation, which mediates navigation. A triaxial gyroscope is sampled concurrently with the on-board video and is used to disambiguate the motion estimates through image derotation. The optical flow algorithm's gains are further tuned using policy gradient reinforcement learning so as to improve motion estimation for specific unsteady regimes. This approach is demonstrated in an obstacle avoidance scenario.

To my family.

Contents

Contents ii

List of Figures iii

List of Tables v

1 Introduction 1

2 Unsteady dynamics of a legged robot 7
2.1 VelociRoACH legged robot and its control policy . . . 7
2.2 Robot dynamics and performance on rough terrain . . . 9
2.3 Steady state running and aerodynamic stabilization . . . 13
2.4 Concluding remarks . . . 15

3 Tuning optical flow estimation 16
3.1 Elementary motion detector . . . 16
3.2 Sensing electronics and sampling characteristics . . . 17
3.3 Comparison between optical flow estimates and gyroscope readings . . . 18
3.4 Estimate scaling factor through reinforcement learning . . . 20
3.5 Concluding remarks . . . 22

4 Disambiguate unsteady optical flow 24
4.1 Locomotion platforms and experimental setup . . . 24
4.2 Looming experiment from the perspective of a single image row over time . . . 26
4.3 Gyroscope-based image derotation . . . 27
4.4 Translation experiment on the VelociRoACH . . . 33
4.5 Looming experiment on the camera dolly . . . 36
4.6 Summary of results . . . 39
4.7 Concluding remarks . . . 41

Bibliography 43

List of Figures

1.1 Running millirobots . . . 1
1.2 Walking millirobots . . . 2
1.3 Specialized millirobots . . . 2
1.4 Gait tuning for legged robots . . . 3
1.5 Performance analysis of legged robots . . . 3
1.6 Visual navigation on-board fixed-wing aircraft . . . 4
1.7 Visual navigation on-board rotorcraft . . . 5
1.8 Visual navigation on-board specialized platforms . . . 5
1.9 Visual navigation on-board a flapping flyer . . . 6

2.1 VelociRoACH robot . . . 8
2.2 Interchangeable surfaces for the experimental test bed . . . 9
2.3 Experimental test bed with interchangeable surfaces . . . 10
2.4 Maximum speed achieved by the robot on three rough terrains . . . 11
2.5 Average frequency spectra of the robot's oscillations on three rough terrains . . . 12
2.6 Robot speed with and without roll stabilizers . . . 13
2.7 Frequency spectra of the robot's oscillations with and without roll stabilizer . . . 14

3.1 Block diagram of three consecutive elementary motion detectors . . . 17
3.2 The 1.3 gram sensing and control board . . . 18
3.3 Axes convention for the sensor board . . . 19
3.4 Comparison between optical flow estimates and gyroscope readings . . . 20
3.5 Optical flow estimates with applied scaling factor versus gyroscope readings . . . 23

4.1 Experimental arena and locomotion platforms . . . 25
4.2 Single row intensity plots and locomotion direction . . . 26
4.3 Block diagram of the image derotation algorithm . . . 27
4.4 Effect of yaw derotation for a VelociRoACH experiment . . . 28
4.5 Effect of pitch derotation for a VelociRoACH experiment . . . 29
4.6 Effect of roll derotation for a VelociRoACH experiment . . . 30
4.7 Derotation effect for a VelociRoACH experiment . . . 31
4.8 Derotation effect for a camera dolly experiment . . . 32

4.9 Translation experiment on the VelociRoACH robot 34
4.10 Translation experiment on the VelociRoACH robot after derotation 35
4.11 Simulation of an oscillating camera in yaw 36
4.12 Simulation of an oscillating camera in yaw after derotation 37
4.13 Looming experiment on the dolly 38
4.14 Looming simulation on a steady platform 39

List of Tables

3.1 Learned scaling parameters 22

4.1 Looming experiment results on the VelociRoACH robot 40
4.2 Looming experiment results for the camera dolly 40

Chapter 1

Introduction

Some modes of locomotion, such as legged walking and flapping flight, are inherently unsteady due to the cyclic interaction of the subject's limbs with a changing and largely unmodelled environment. Bio-inspired robots that locomote this way, present a unique challenge to indoor navigation because the sensors used for exteroception record this unsteadiness in their readings.

Millirobotic crawling platforms are great examples of unsteady robots. They have in general been optimized from a design perspective at the mechanical level to excel at a certain behavior. Sprinting drove the development of DASH (Birkmeyer, Peterson, and Fearing 2009), DynaRoACH (Hoover, Burden, et al. 2010), and VelociRoACH (Haldane et al. 2013) (see Figure 1.1); walking underpinned it for RoACH (Hoover, Steltz, and Fearing 2008), MEDIC (N. J. Kohut et al. 2011), HAMR^3 (Baisch et al. 2011), and Harvard's Myriapod (Hoffman and R. J. Wood 2011) (see Figure 1.2); climbing drove it for CLASH (Birkmeyer, Gillies, and Fearing 2011); hybrid locomotion for DASH+Wings (Peterson, Birkmeyer, et al. 2011) and BOLT (Peterson and Fearing 2011); turning drove development for OctoRoACH (Pullin et al. 2012) and TAYLRoACH (N. Kohut et al. 2013); and sprawling underpinned STAR (Zarrouk et al. 2013) (see Figure 1.3). What was not often reported, though, is that although the designs may have been optimal for a specific task, manufacturing variability

(a) DASH **(b)** DynaRoACH **(c)** VelociRoACH

Figure 1.1: Running millirobots.

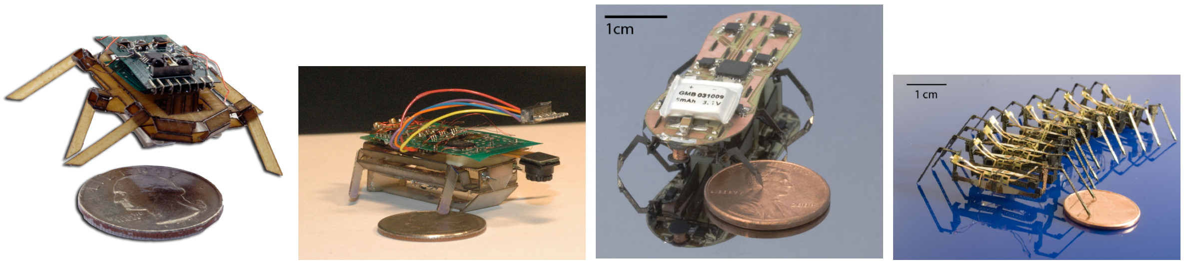

(a) RoACH **(b)** MEDIC **(c)** HAMR^3 **(d)** Harvard's Myriapod

Figure 1.2: Walking millirobots.

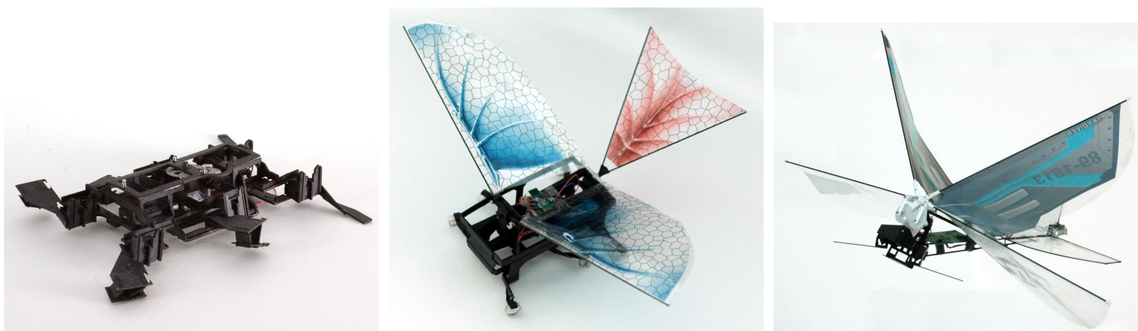

(a) CLASH **(b)** DASH+Wings **(c)** BOLT

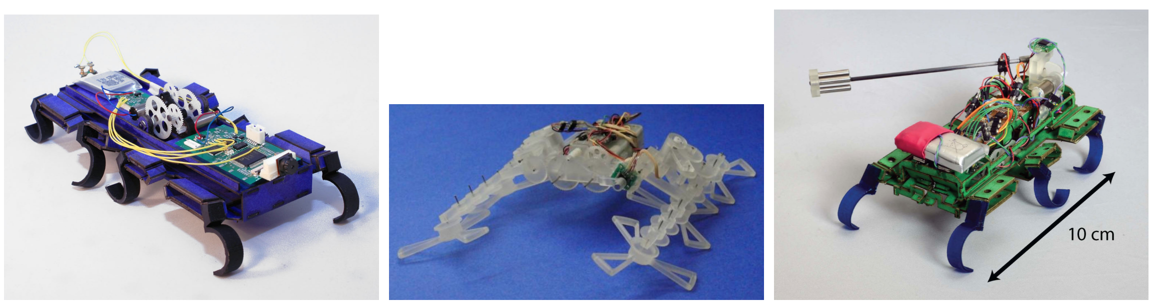

(d) OctoRoACH **(e)** STAR **(f)** TAYLRoACH

Figure 1.3: Specialized millirobots.

can result in poor performance. This is even more significant at the millirobot scale and was a particularly crucial limitation of the actuation mechanism of the Micromechanical Flying Insect (Avadhanula et al. 2003). Improved manufacturing capabilities was crucial for achieving the first controlled flight of an insect-scale flapping robot (Ma et al. 2013).

Several groups have worked on adapting their robot's gait to achieve better performance at tasks the robot was not designed for (e.g. walking on granular media instead of hard ground (Li, Umbanhowar, et al. 2009)) or to achieve better performance than that achieved solely through hand tuning (Weingarten et al. 2004) (see Figure 1.4). Although the above adaptation strategies implied changing the leg motion profile, more passive solutions, such as tuning the leg stiffness, have been attempted with moderate success (Galloway et al.

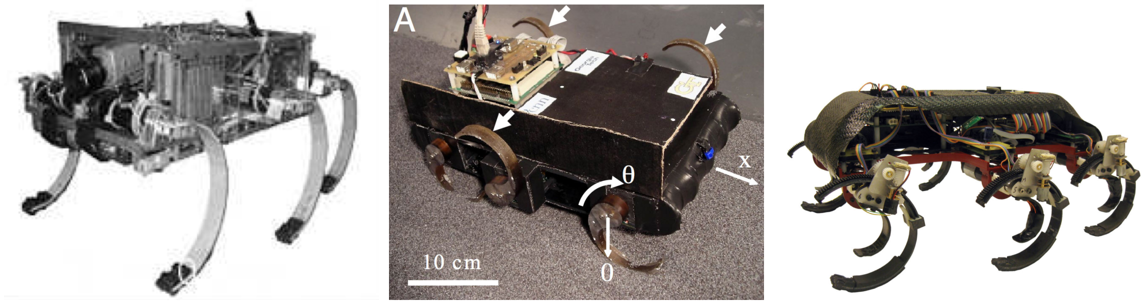

(a) RHex **(b)** SandBot **(c)** EduBot

Figure 1.4: Gait tuning for legged robots.

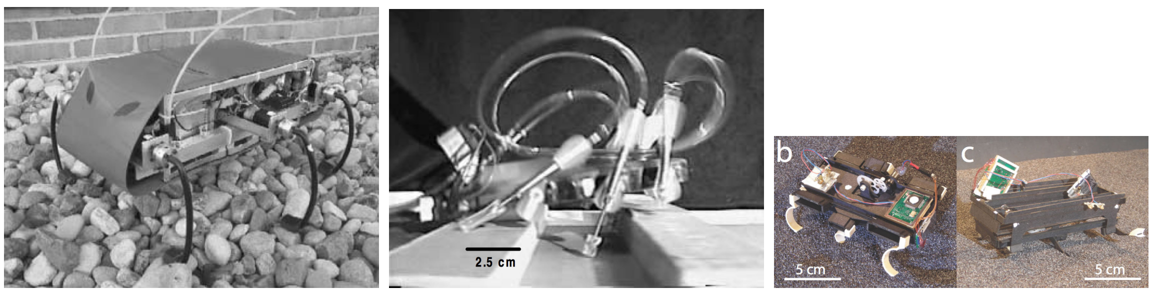

(a) Original RHex **(b)** Sprawlita **(c)** DynaRoACH and DASH

Figure 1.5: Performance analysis of legged robots.

2011; Hoover, Burden, et al. 2010). Minimal actuation presents yet another obstacle for gait adaptation, since the robot can have a number of uncontrollable dynamic modes. In contrast, many large robots depend on either extensive actuation or precise sensors in order to traverse their environment (Espenschied et al. 1996; Kolter, Rodgers, and Ng 2008).

Robust indoor navigation of an unsteady robot is still a challenging problem due to the constrained environment and abundant nearby obstacles that buildings, both collapsed and standing, present. Insects such as flies succesfully negotiate clutter using flapping wings, which allow for complex maneuvering at high acceleration rates (Dickinson, Lehmann, and Sane 1999). Their small size also enables them to traverse tiny openings with ease. Based on these biological insights, ornithopters have been developed at the scale of insects (Avadhanula et al. 2003; Ma et al. 2013; R. J. Wood 2008) and small birds (Lentink, Jongerius, and Bradshaw 2010).

Conventionally, robots rely on GPS for localization, but this is unreliable indoors due to weaker or non-existent satellite signals. Instead, lightweight laser rangefinders have succesfully been integrated into robots with the required payload capacity, such as quad-rotors (Bachrach, He, and Roy 2009). Insects present an alternative approach, inspiring the use of low-resolution vision sensors (Land 1997) for optical flow motion estimation (Egelhaaf and Reichardt 1987). Several research groups have implemented optical flow navigation for indoor flying robots such as fixed-wing aircrafts (Barrows, Chahl, and Srinivasan 2002;

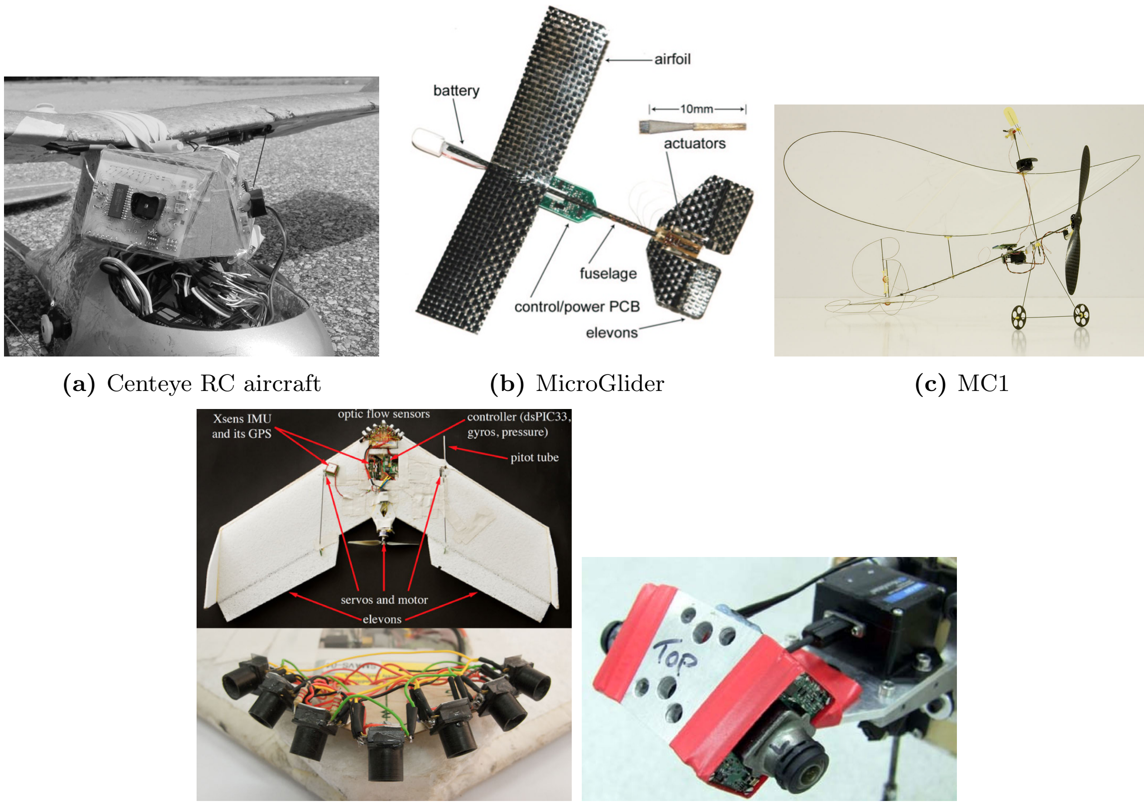

(a) Centeye RC aircraft **(b)** MicroGlider **(c)** MC1

(d) optiPilot swinglet **(e)** QBI's wind-field estimator

Figure 1.6: Visual navigation on-board fixed-wing aircraft.

Beyeler, Zufferey, and Floreano 2007; Moore, Thurrowgood, and Srinivasan 2012; R. Wood et al. 2005; Zufferey, Beyeler, and Floreano 2010; Zufferey and Floreano 2006) (see Figure 1.6), tethered (Expert and Ruffier 2012; Kerhuel, Viollet, and Franceschini 2010; Ruffier and Franceschini 2005) and untethered helicopters (Barrows, Chahl, and Srinivasan 2002), quad-rotors (Conroy et al. 2009; Herisse et al. 2010; Zingg et al. 2010) (see Figure 1.7), and airships (Iida 2003; Zufferey, Guanella, et al. 2006). On a similar vein, other groups have implemented optical flow on wheeled robots (Srinivasan et al. 2004), a gantry (Reiser and Dickinson 2003), and motors (Plett et al. 2012).

Optical flow implemented on-board a flapping wing robot usually suffers from the platform's inherent unsteadiness (de Croon et al. 2010; Garcia Bermudez and Fearing 2009). Flies, on the other hand, are capable of flexing their head with respect to their thorax, which might help them passively dampen flapping oscillations (van Hateren and Schilstra 1999). The active rotation of their head can also serve for gaze stabilization (Huston and Krapp 2008). These insights inspire mechanical solutions such as gimbal mechanisms and active motor-based dampers that are generally too heavy for a lightweight flying robot. Millirobots flapping at frequencies closer to those of winged insects, like the RoboBee (Duhamel et al. 2012), might be passively damping their flapping oscillations using their body's inertia.

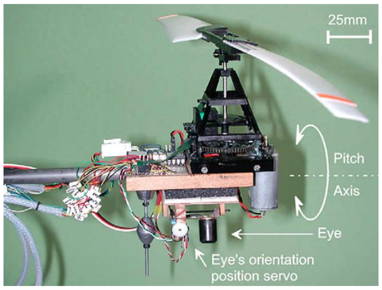

(a) OCTAVE autopilot

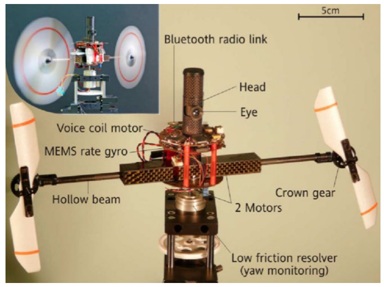

(b) OSCAR II

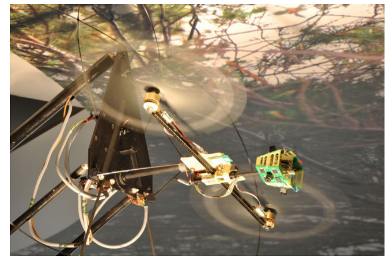

(c) BeeRotor

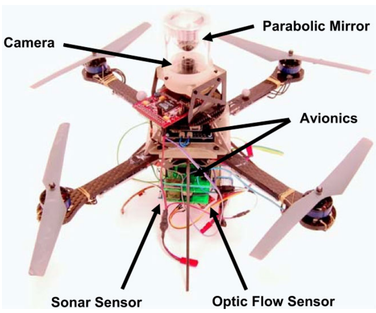

(d) UMD autonomous quad-rotor

(e) μEye

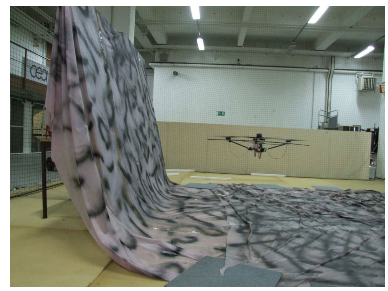

(f) VTOL terrain follower

Figure 1.7: Visual navigation on-board rotorcraft

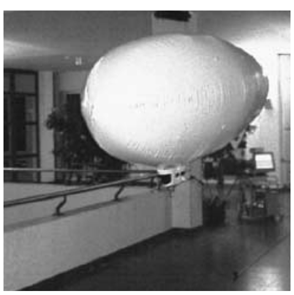

(a) Melissa

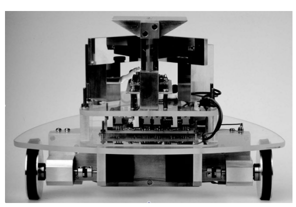

(b) Corridor follower

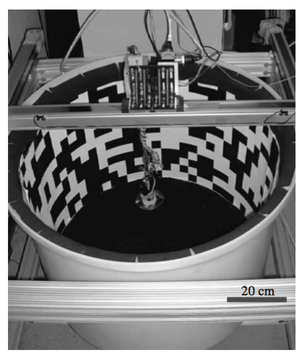

(c) FlyBall

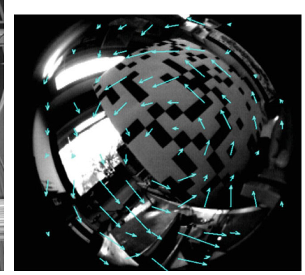

(d) Motorized SmartCam

Figure 1.8: Visual navigation on-board specialized platforms.

Other flapping platforms that can visually navigate their environments include a modified iBird (Baek, Garcia Bermudez, and Fearing 2011) and AeroVironment's NAV.

The optical flow algorithm chosen for this work is the correlation-based elementary motion detector (EMD) (Hassenstein and Reichardt 1956; Reichardt 1961), which is widely believed to underlie motion computation in flies (Egelhaaf and Reichardt 1987; Franceschini, Riehle, and Le Nestour 1989; Haag, Denk, and Borst 2004). Recent work provides further evidence of the mapping between neurobiological processes and the different stages of the EMD algorithm (Joesch et al. 2013; Maisak et al. 2013). The EMD has an inherent capacity for adapting to different velocity ranges, a feature not present in algorithms based

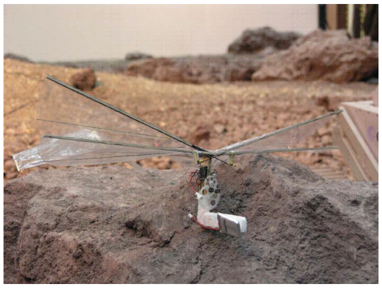

(a) DelFly

(b) DelFly II

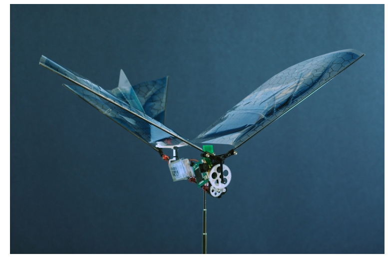

(c) Modified Vamp

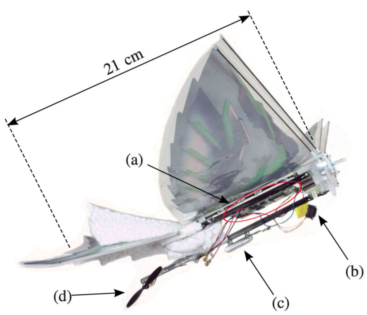

(d) Modified iBird

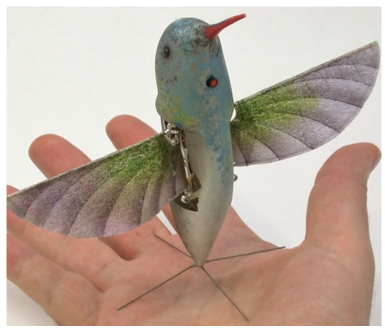

(e) AeroVironment's NAV

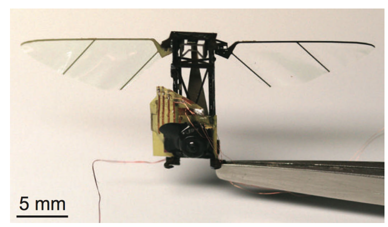

(f) RoboBee

Figure 1.9: Visual navigation on-board a flapping flyer.

on gradient techniques (Borst 2007), that enables the EMD to work over a wide range of signal-to-noise ratios. Brinkworth and O'Carroll (2009) propose one of the most efficient motion detection algorithms for use in high dynamic range natural scenarios, which builds on the EMD. Based on biological observations, they add slightly more computationally complex pre- and post-processing of the data and underscore the importance of a large field of view.

Chapter 2 focuses on the performance analysis of the VelociRoACH legged robot, which we chose for experimentation. Similar analysis were done for RHex (Saranli, Buehler, and Koditschek 2001), Sprawlita (Cham, Karpick, and Cutkosky 2004), and both DASH and DynaRoACH (Li, Hoover, et al. 2010) (see Figure 1.5). Without adapting gait, we investigate how varying the stride frequency has an effect on locomotion over three distinct rough terrains. Chapter 3 focuses on sensing characteristics and optical flow estimation while Chapter 4 deals with extracting exteroceptive information from the optical flow estimates captured on-board both steady and unsteady locomotion platforms. We also compare the output of smooth and oscillating 2D and 3D simulations to that obtained from equivalent experiments.

Chapter 2

Unsteady dynamics of a legged robot

In this chapter, we investigate the dynamics and performance of a legged robot as it traverses three distinct rough terrains: tile, carpet, and gravel. We then focus on the rotational dynamics of the robot with and without an aerodynamic stabilizer as it locomotes across carpet. We find that precise tuning of the leg compliance is key to increased performance on a particular terrain because the robot dynamics are greatly effected by terrain interactions. We also find that roll oscillations dominate the dynamics and that the addition of an aerodynamic stabilizer filters these oscillations at higher stride frequencies. This work has been published in Garcia Bermudez, Julian, et al. 2012 and Haldane et al. 2013 that are copyrighted © IEEE.

2.1 VelociRoACH legged robot and its control policy

The VelociRoACH is a newly designed six-legged dynamic running robot (ibid.), pictured in Figure 2.1, which is based on the OctoRoACH (Pullin et al. 2012) and DASH (Birkmeyer, Peterson, and Fearing 2009) robot designs. It features an inboard dual drive-train for independent control of the right and left set of legs. Its SCM fabricated (Hoover and Fearing 2008) transmission is highly rigid due to planarizing parallel four-bar linkages which couple the drive-train output crank to kinematic linkages that govern the motion of the legs. We expect this increased rigidity to isolate the compliance of the system to the deformable polymeric legs, allowing for more predictable and repeatable dynamic terrain response. The overall mass of the robot, with battery, is 29.1 grams and it can attain a maximum stride frequency of 24 Hz.

The robot is driven by embedded sensing and control hardware (Baek, Garcia Bermudez, and Fearing 2011), which includes an inertial measurement unit and an 802.15.4 wireless radio for issuing control commands and downloading telemetry data[1]. Unlike in previous work (Pullin et al. 2012), where the on-board controller was mainly dependent on the motors'

[1]Embedded board: https://github.com/biomimetics/imageproc_pcb

Figure 2.1: VelociRoACH robot, outfitted with motion capture tracking dots, positioned on top of the gravel used for experimentation.

back-electromotive force (back-EMF), the current robot adds magnetic encoders to each motor, enabling control of the relative phasing between the two alternating tripods[2].

The kinematic linkages described previously effectively define a hardware-based Buehler clock (Seipel and Holmes 2007), in which the touchdown and liftoff angles ($\phi_{TD,LO} = \pm 42°$) and duty cycle ($\delta = 0.5$) are rigidly defined by the geometric parameters of the four-bar linkages (Hoover, Burden, et al. 2010). Therefore, from the controller side, the Buehler clock becomes defined by one parameter: the stride period, t_c, or inversely the stride frequency, f_c.

To assess the VelociRoACH's rough terrain performance, we varied its stride frequency when traversing laminate tile, gravel, and medium-pile carpet (see a picture of each surface in Figure 2.2). The dimensions of the experimental test bed are $1.14\,\mathrm{m} \times 1.75\,\mathrm{m}$. Ground truth data was collected using an OptiTrack[3] motion capture system comprised of eight V100:R2 cameras located .45 m above the terrain and capable of sub-millimeter accuracy as specified

[2]Embedded code: https://github.com/biomimetics/octoroach
[3]NaturalPoint, Inc. OptiTrack: http://www.naturalpoint.com/optitrack/

(a) (b) (c)

Figure 2.2: Interchangeable surfaces for the experimental test bed: (a) laminate tile, (b) gravel, and (c) medium-pile carpet.

by the manufacturer. Figure 2.3 shows the experimental test bed with interchangeable surfaces and the OptiTrack system.

2.2 Robot dynamics and performance on rough terrain

The performance metric used for the experiments in this section is the robot's maximum speed as it traverses each terrain, which was calculated from the 3-D position data that the OptiTrack provides. Note that since the robot was not controlled for heading, the trajectories it took need not have been straight, particularly given that leg-ground interactions can substantially alter its direction. Nonetheless, the generalized traversal speed was computed using Python[4] from the ℓ^2-norm of the instantaneous position changes.

[4]Scientific Tools for Python: http://www.scipy.org/

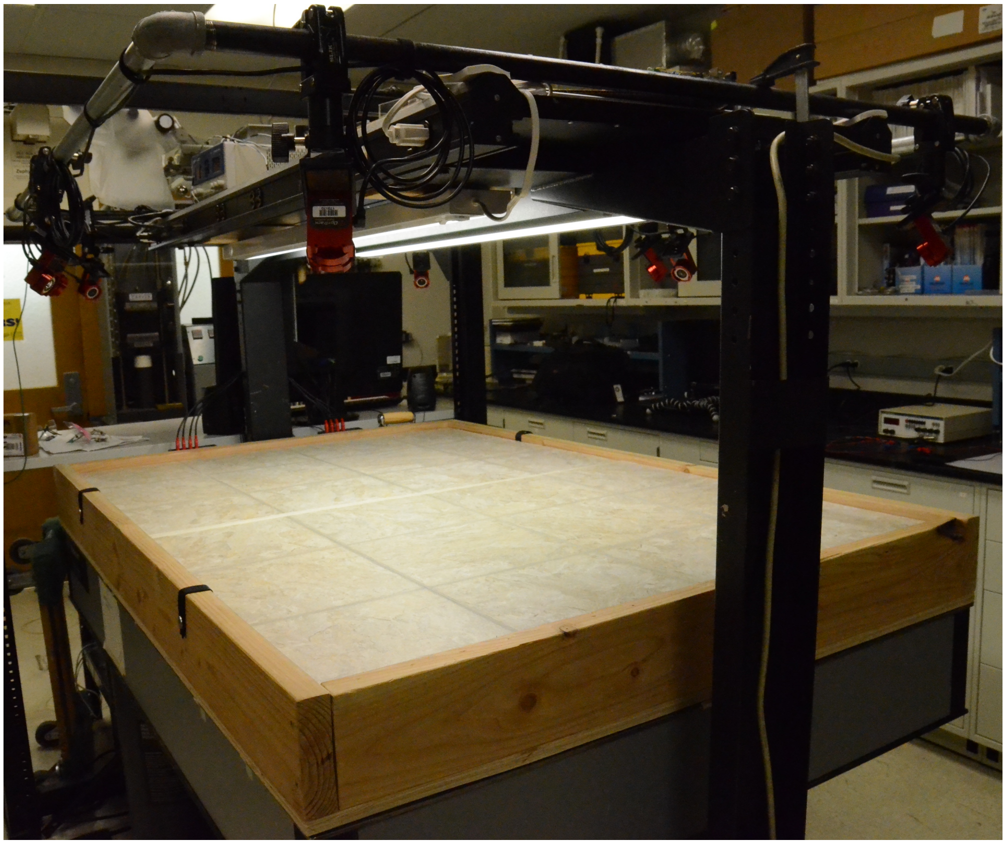

Figure 2.3: Experimental test bed with interchangeable surfaces and an eight-camera OptiTrack motion capture system.

For each individual run, the robot's legs were always started from the same position within their cycle. The position and orientation of the robot were not reset for each individual run. We always monitored that the legs were indeed successfully reset before a new run was started, if not the case, we moved them into place by hand.

Performance as a function of stride frequency

To gain a better understanding of how stride frequency variation affects the robot's performance on the three terrains, we ran a parameter sweep on f_c of 1–11 Hz in steps of 1 Hz. Figure 2.4 shows a plot of the maximum speed achieved at each stride frequency, along with a one standard deviation error bar. Each f_c setting was repeated five times ($n = 5$) and the resulting maximum speeds are shown as a scatter plot in the background.

The deformable polymeric legs of the robot are tuned for best performance on hard ground, which explains why it achieves the greatest speeds on tile. This comes at a cost for our experiments, though, given the limited size of our test bed. Starting at about 6 Hz, the increased variance corresponds to the robot not always reaching its maximum speed while

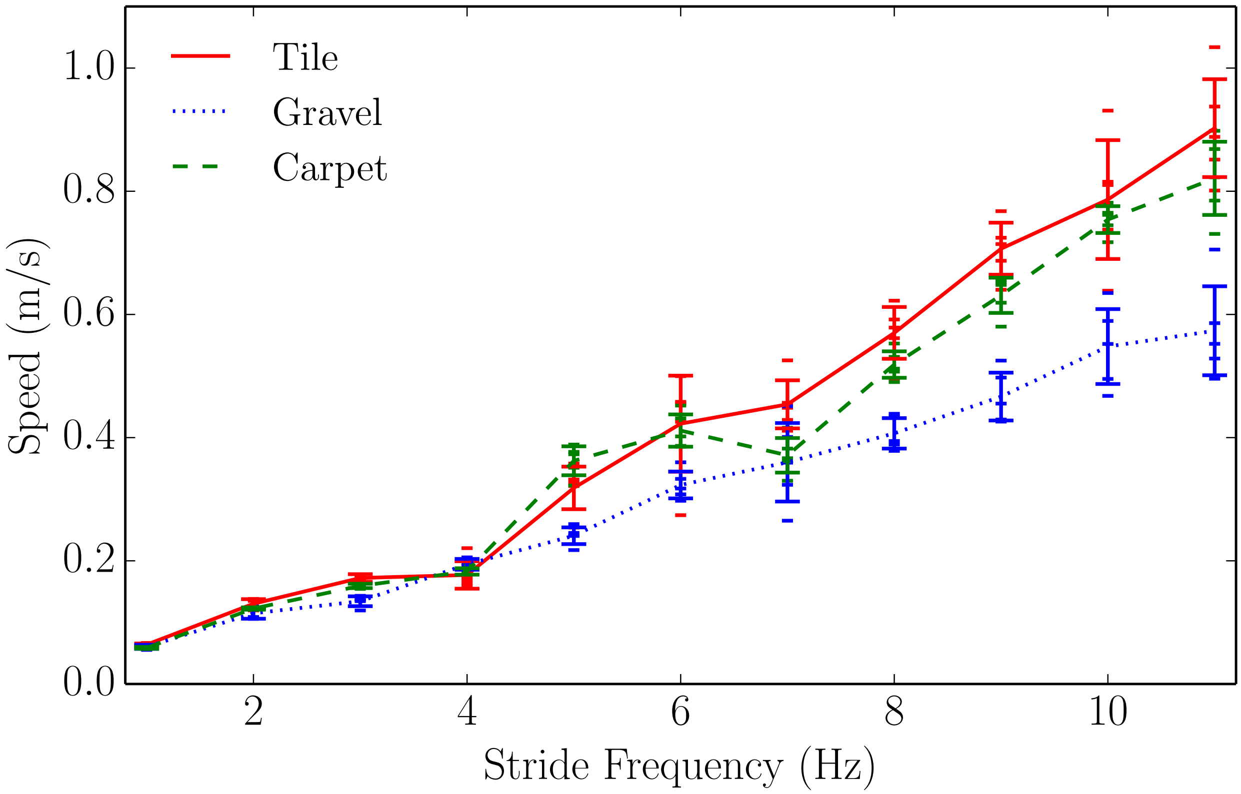

Figure 2.4: Maximum speed achieved by the robot on three rough terrains as a function of the stride frequency ($n = 5$), along with a one standard deviation error bar. The raw data is plotted as a scatter plot in the background. Note that the best performance is achieved on tile and is closely followed by that on carpet. The robot runs the worst on gravel, yet note the dips in performance for the other terrains at 4 and 7 Hz. These correspond to larger roll oscillations visible in Figure 2.5.

inside the tracking volume. The reported speed is thus a lower bound on the maximum achievable at those stride frequencies.

Apart from two dips in performance at 4 and 7 Hz, the robot's speed increased with stride frequency on all terrains. The performance on carpet follows that of tile, but at a reduced overall speed (which is not statistically significant). Since the carpet's surface is more compliant than that of tile, the polymeric legs could require stiffening so as to achieve the same overall compliance between the robot and the terrain (Ferris, Louie, and Farley 1998), thus improving its performance.

The lower speeds on gravel can be attributed to its fluidity. The gravel rocks are roughly the size of the VelociRoACH's feet (see Figure 2.1) and as it moves over the terrain, the legs will either scoop rocks around or the robot's feet will yield into the surface, impeding traction. As shown in previous studies of robot locomotion on fluidizing ground, leg dynamics tuned for hard ground generally need to be modified to achieve decent performance on flowing terrains (Li, Hoover, et al. 2010; Li, Umbanhowar, et al. 2009; Qian et al. 2012).

Figure 2.5 is a plot of the frequency spectra of the robot's oscillations in the body frame

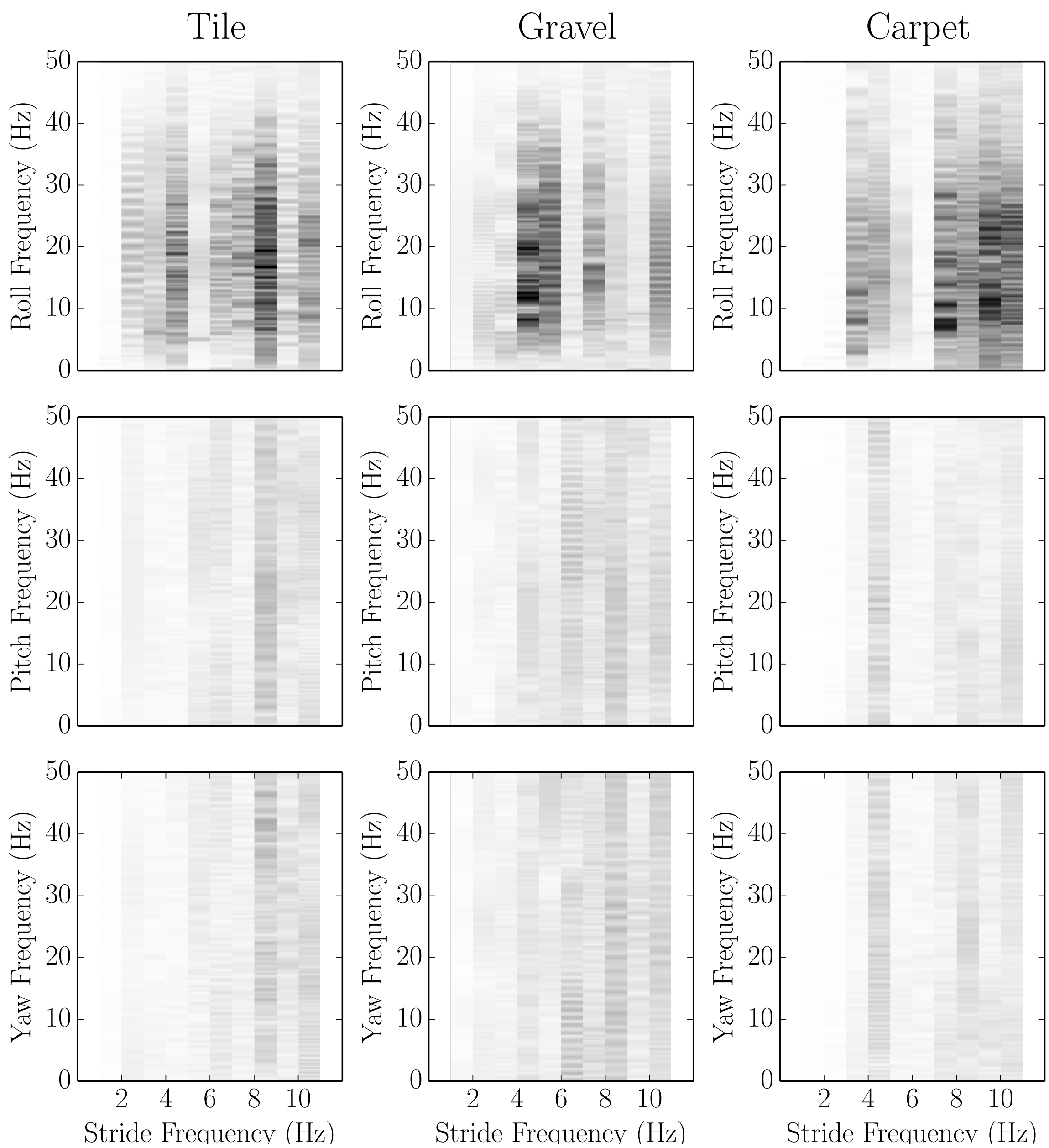

Figure 2.5: Average frequency spectra of the robot's oscillations on three rough terrains as a function of the stride frequency ($n = 5$). Note how roll oscillations dominate the dynamics and, in particular, how larger oscillations generally correlate to the dips in performance seen in Figure 2.4.

as a function of the stride frequency. The spectra are averaged across the five sample runs taken at each stride frequency. Note that the larger oscillatory peaks correspond to the robot's roll dynamics. In particular, the roll frequency spectra on tile has distinct peaks at 4 and 7 Hz, which correspond to the dips in performance visible in Figure 2.4. Since these frequencies excite large roll oscillations on the robot, some of the locomotive energy will be

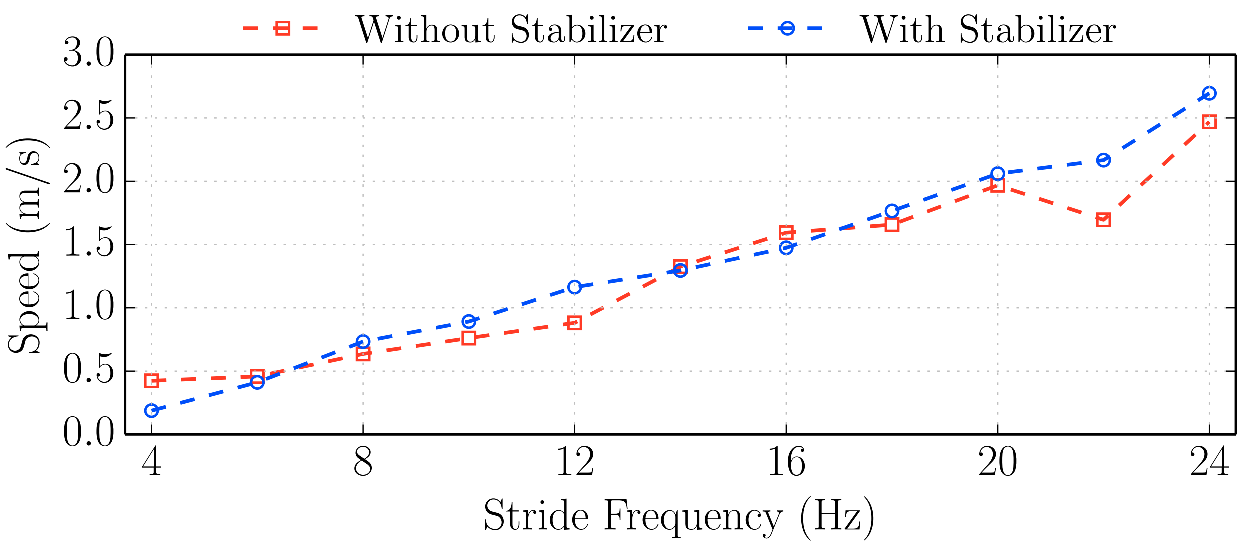

Figure 2.6: Robot speed with and without roll stabilizers as a function of the commanded stride frequency. Note that there's no measurable effect from the stabilizers on the forward progress of the robot.

expended oscillating instead of running forward and the performance is thus reduced (Clark and Cutkosky 2006). On carpet, the reduced performance at higher stride frequencies can now be understood in relation to the larger roll oscillations above 6 Hz, probably caused by the excessive compliance in the leg-ground interactions. The flowing gravel, on the other hand, might be helping dampen oscillations, but the corresponding loss of traction guarantees reduced locomotive speed.

2.3 Steady state running and aerodynamic stabilization

The performance analysis of the robot traversing different rough terrains has highlighted the importance of leg tuning and its relationship to terrain characteristics, such as its compliance. To push the robot's performance to its current limits, this section presents experiments done over closed-loop carpet with legs specifically tuned to this terrain. The rotational dynamics of the robot are further characterized and a roll aerodynamic stabilizer is introduced to improve the robot's stability at high speeds. Telemetry and Vicon[5] motion capture data was recorded for the VelociRoACH robot running at stride frequencies in the 4–25 Hz range.

Figure 2.6 shows the speed of the robot as a function of commanded stride frequency. The aerodynamic stabilizer improves the robot's reliability at the higher speeds, with zero incidents of catastrophic destabilization, which were occasionally observed in the unmodified configuration. There is no measurable effect from the stabilizers on the forward progress of

[5]Vicon Motion Capture Systems: http://www.vicon.com/

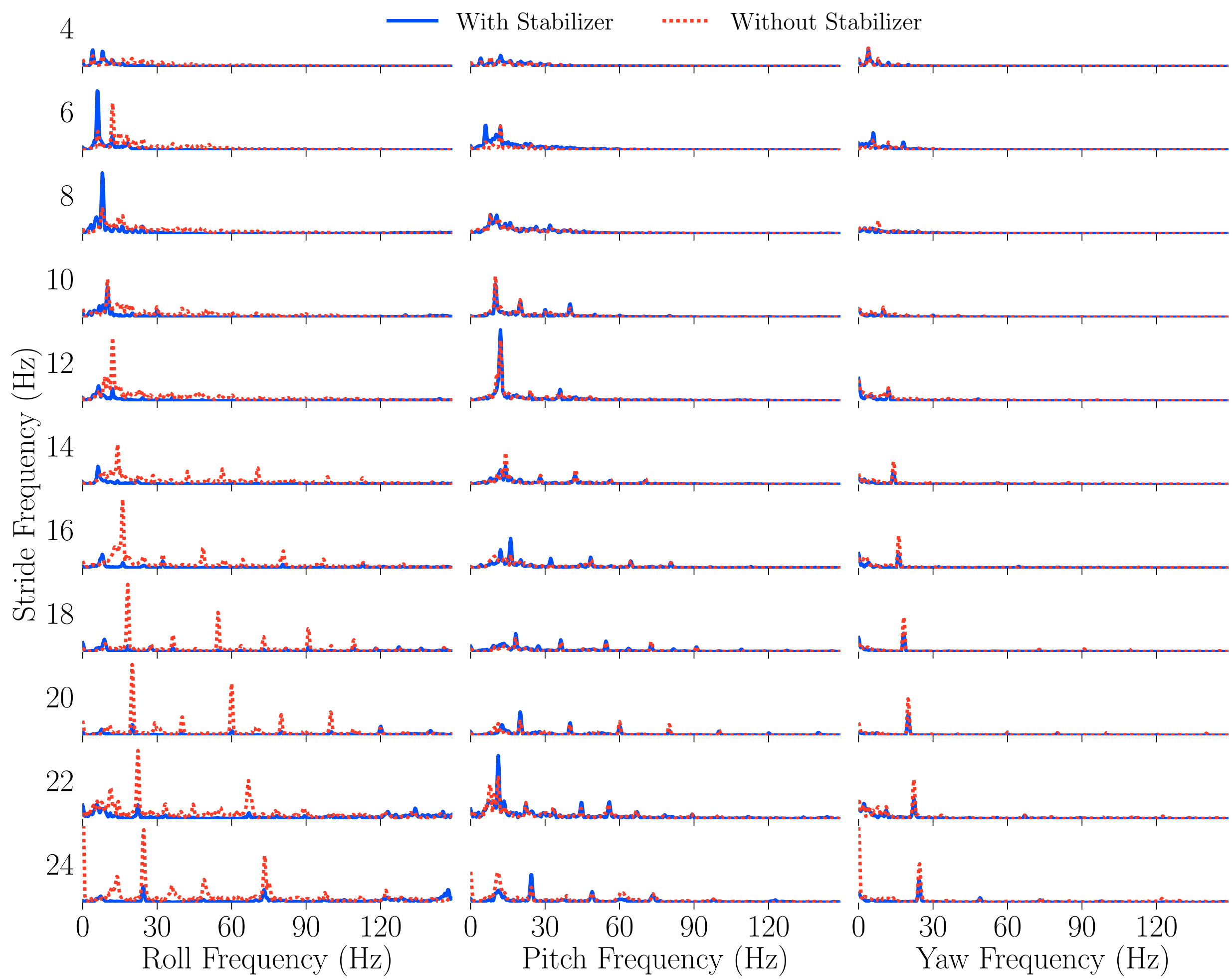

Figure 2.7: Frequency spectra of the robot's oscillations with and without roll stabilizer plotted as a function of the commanded stride frequency. Oscillatory energy in the roll axis was the highest of all the rotational components prior to the addition of the stabilizer. The stabilizer effectively filters this energy at higher stride frequencies. Both pitch and yaw are relatively unaffected by the added stabilizer.

the robot. The addition of the roll stabilizer did not slow the robot, as might have been expected from additional aerodynamic drag.

As part of the telemetry, tri-axial gyroscope data was logged at 300 Hz during each run (repeated three times). We discarded the leading one second of each trial to remove any transient effects. To better understand the nature of the VelociRoACH oscillations as a function of the stride frequency, we used Python to compute the fast Fourier transform of each run, first passed through a Hann window, and then averaged across repeated trials. The resulting frequency spectra are plotted for pitch, roll, and yaw in Figure 2.7. Roll shows a large degree of oscillation without the stabilizer, visible throughout the spectra and reaching up to the fifth harmonic of the commanded stride frequency. This motivated the addition of the stabilizer on the roll axis, and Figure 2.7 shows this approach was successful at reducing the degree of roll oscillations. Both pitch and yaw, which have less oscillations to begin with, are relatively unaffected by the added stabilizer.

2.4 Concluding remarks

The experimentation and analysis presented in this chapter has underscored the unsteady characteristics of the VelociRoACH legged robot as it locomotes over rough terrain. Precise tuning of the leg compliance is key to increased performance on a particular terrain because the robot dynamics are greatly effected by the leg-ground interactions. Roll oscillations were found to dominate the dynamics and the addition of an aerodynamic stabilizer was effective at preventing catastrophic destabilization at higher stride frequencies.

Chapter 3

Tuning optical flow estimation

In this chapter, we delve into the optical flow algorithm chosen and the sensor capture board's sampling characteristics. We then compare optical flow estimates to gyroscope readings in an experiment that involves camera rotations against a distant background and find the scaling factor between the two signals through optimization.

3.1 Elementary motion detector

The elementary motion detector (EMD) optical flow algorithm (Hassenstein and Reichardt 1956; Reichardt 1961), which is displayed in Figure 3.1 as a block diagram, is described by the following equation for a local pixel patch transitioning from frame k to $k+1$:

$$\vec{v}_{i,j}(k) = \begin{bmatrix} u_{i,j}(k) \\ v_{i,j}(k) \end{bmatrix} = \begin{bmatrix} i_{i,j}(k+1)\ i_{i+1,j}(k) - i_{i+1,j}(k+1)\ i_{i,j}(k) \\ i_{i,j}(k+1)\ i_{i,j+1}(k) - i_{i,j+1}(k+1)\ i_{i,j}(k) \end{bmatrix},$$

where $\vec{v}_{i,j}(k) = [u_{i,j}(k), v_{i,j}(k)]^T \in \mathbb{R}^2$ is the (i,j)th element of the optical flow vector field, $\vec{V}$, with horizontal and vertical components, $U, V \in \mathbb{R}^{(m-1)\times(n-1)}$. $I \in \mathbb{N}_0^{m\times n}$ is the pixel intensity matrix.

The output of individual EMDs is composed of a direct current (DC) component, corresponding to the stimulus motion direction; and an alternating current (AC) component, that follows the local light intensity modulations (Haag, Denk, and Borst 2004). The AC component carries no directional information and is phase-shifted with respect to neighboring EMDs (ibid.). Therefore, spatial integration and normalization of many adjacent EMDs should just preserve the directional DC component:

$$\vec{v_{int}}(k) = \begin{bmatrix} u_{int}(k) \\ v_{int}(k) \end{bmatrix} = \left[\frac{\sum_{i,j} u_{i,j}(k)}{\|U(k)\|_2}, \frac{\sum_{i,j} v_{i,j}(k)}{\|V(k)\|_2} \right]^T,$$

where $\vec{v_{int}}(k) = [u_{int}(k), v_{int}(k)]^T \in \mathbb{R}^2$ is the integrated and normalized optical flow field. This computation is supported by biological observations of the fly's nervous system (Single and Borst 1998).

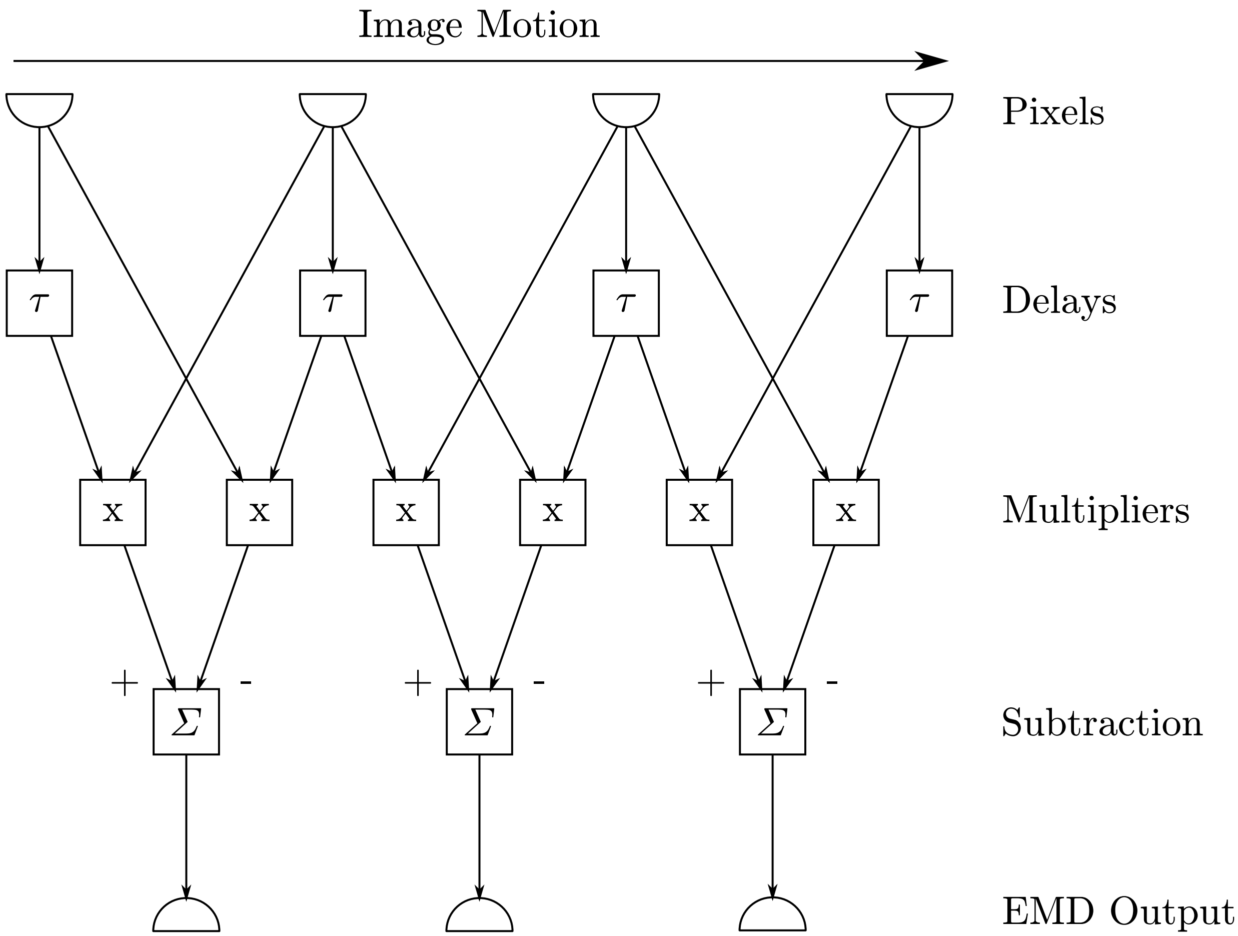

Figure 3.1: Block diagram of three consecutive elementary motion detectors (adapted from Reichardt 1987).

3.2 Sensing electronics and sampling characteristics

The custom-made sensing and control board[1], first introduced in Baek, Garcia Bermudez, and Fearing (2011), is shown in Figure 3.2. The board weighs 1.3 grams and consists of a Microchip 16-bit dsPIC microprocessor running at 40 MHz, an OmniVision OV7660FSL VGA monocular camera, a 4 MB flash memory, a 3-axis gyroscope, an 802.15.4 wireless transceiver, and a 2-channel detachable motor driver.

The camera has a framerate of 25 Hz and is setup for 160 pixels $\times$ 120 pixels (QQVGA) resolution. From the 160 pixels of each row, only the center 152 pixels are kept. We do this to maximize the number of samples that can be stored on a flash page, which in turn allows us to achieve a higher sampling frequency. From the 120 rows of each frame, only 1 in every 4 rows is kept, resulting in a total of 30 rows per frame. We do this to accomodate the sampling of the gyroscope and the transmission of all these signals to flash storage.

[1]Embedded board: https://github.com/biomimetics/imageproc_pcb

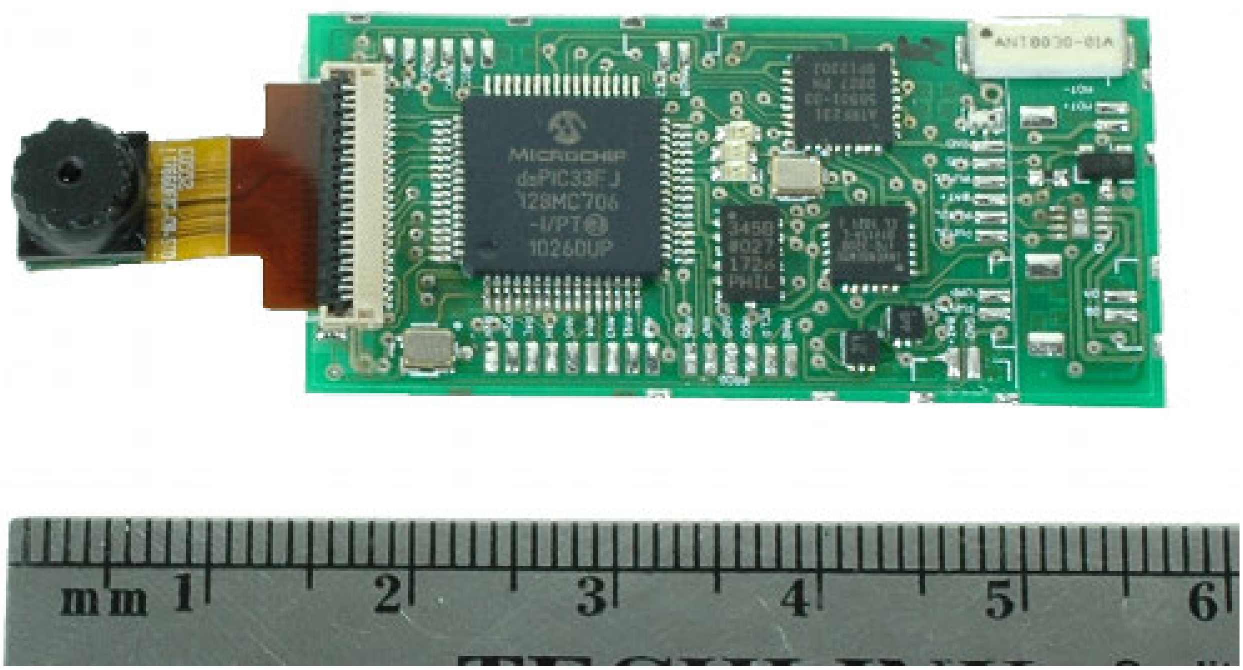

Figure 3.2: The 1.3 gram sensing and control board consists of a 40 MHz dsPIC microprocessor, a monocular camera, 4 MB of flash memory, a 3-axis gyroscope, an 802.15.4 wireless transceiver, and a 2-channel motor driver.

The resulting images have a resolution, $m \times n$, of 152 pixels $\times$ 30 pixels. Their rows are captured asynchronously at 2 kHz and tagged with a timestamp of microsecond resolution. The triaxial gyroscope is calibrated before each experimental run, sampled at 1 kHz, and also tagged with a timestamp. At the end of an experiment, all captured data is wirelessly transmitted to the host computer for off-board processing.

Figure 3.3 illustrates how the axes convention for the camera matches that of the gyroscope. When transforming from the camera frame to the image frame, the u dimension follows the same sign convention as the yaw axis, but the v dimension is inverted with respect to the pitch axis.

3.3 Comparison between optical flow estimates and gyroscope readings

Optical flow estimates resulting from the EMD algorithm don't immediately represent physical quantities. They are a measure of the relative motion of the camera with respect to its environment, but are subject to scale ambiguity. Given that we carry a triaxial gyroscope on-board, we can resolve this ambiguity by performing experiments where the camera motion

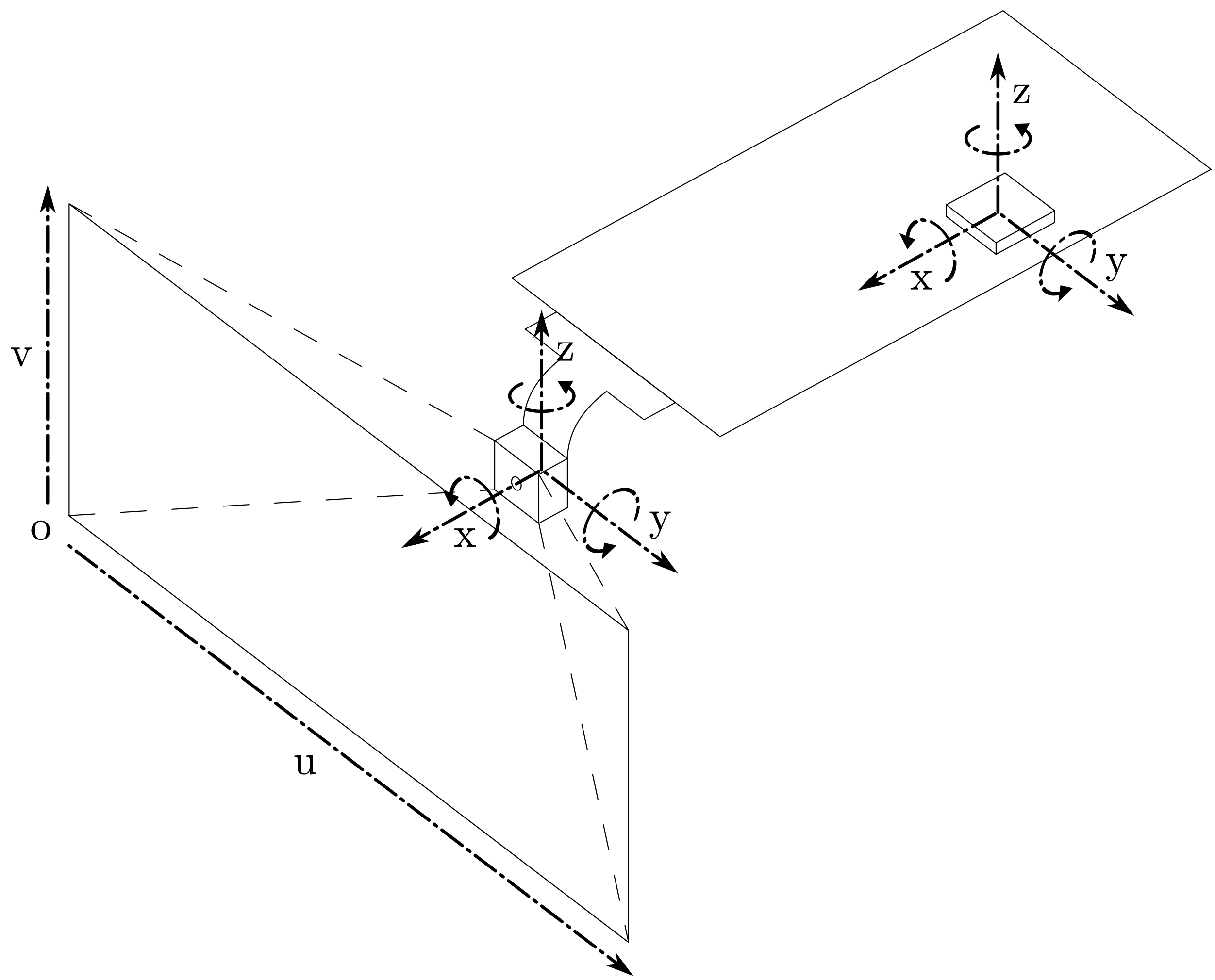

Figure 3.3: Axes convention for the sensor board. Note that the camera and gyroscope have matching axes for roll, pitch, and yaw. In the image frame, U follows the same sign convention as the yaw axis, but V is inverted with respect to the pitch axis.

is overwhelmingly rotational and then finding the scaling factor between the two signals.

One such experiment is introduced in Section 4.4 and involves the VelociRoACH legged robot (Haldane et al. 2013) slowly translating forward against the distant background texture of the laboratory. Figure 3.4 shows the typical output of one such experiment. The top plot displays the on-board video sequence as the robot slowly locomotes forward, while the other three plots display the rotational rates as measured by the gyroscope and estimated by the optical flow algorithm in yaw, pitch, and roll.

The linearly-interpolated integrated optical flow signals, u_{int} and v_{int}, are reasonably well correlated to the corresponding gyroscope measurements, with correlation coefficients of 65.5% and 59.3%, respectively. As expected, though, there is a difference in magnitude between the optical flow estimates and the gyroscope readings, which we will estimate in the

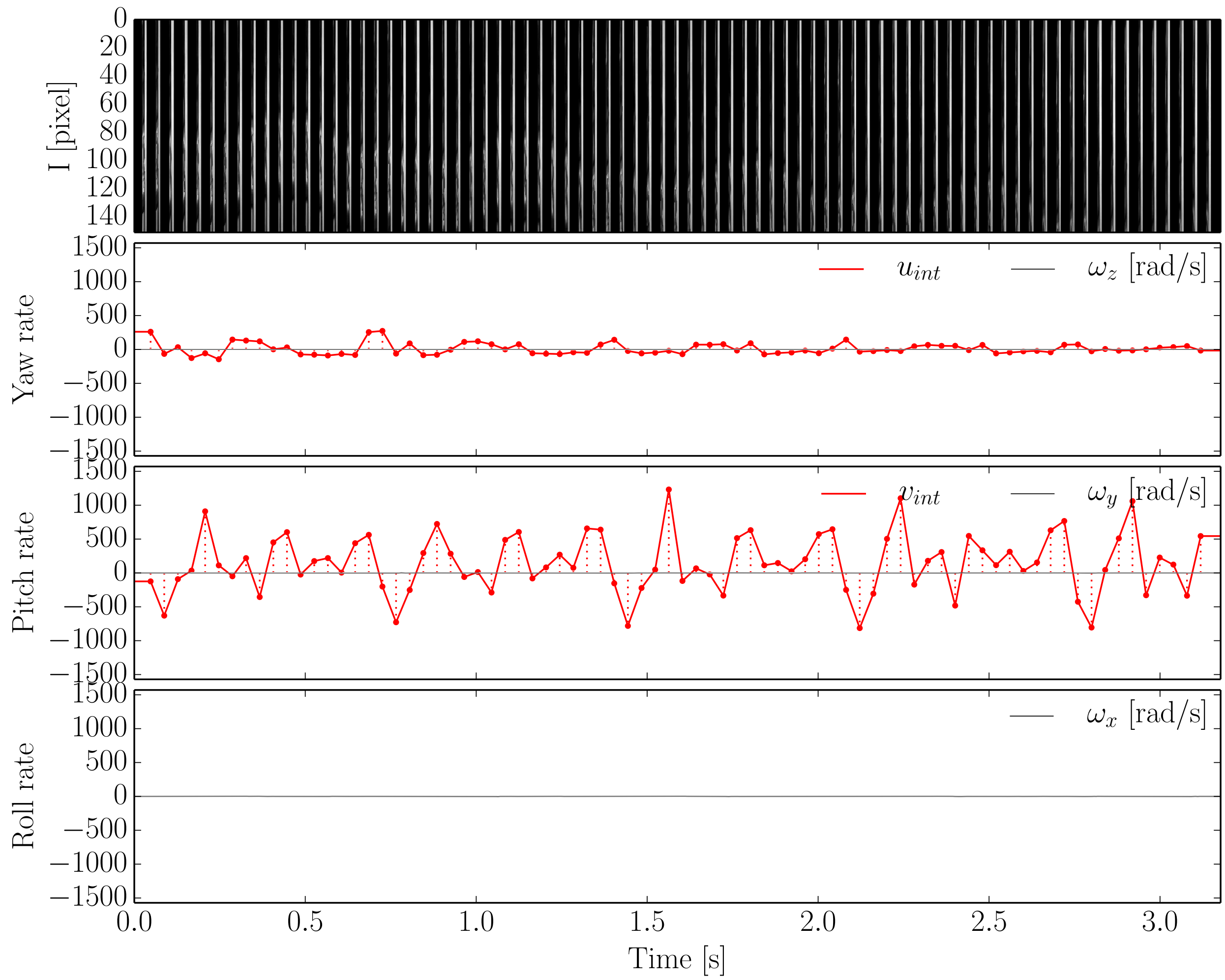

Figure 3.4: Comparison between optical flow estimates and gyroscope readings for an experiment where the VeloiRoACH robot slowly translates forward against a distant background. The video sequence captured by the on-board camera is plotted at the top, while the rotational rates as measured by the gyroscope and estimated by the optical flow algorithm are plottled in the bottom three plots for yaw, pitch, and roll. Note the difference in magnitude between the optical flow estimates and the corresponding gyroscope readings.

following section.

3.4 Estimate scaling factor through reinforcement learning

The scaling factor between the optical flow estimates and the gyroscope readings can be estimated through optimization. For this purpose, we use a policy gradient reinforcement learning framework (see Peters and Schaal 2006, for a review) that has the goal of optimizing policy parameters, $\theta \in \mathbb{R}^p$, so that the expected return is optimized with respect to the average reward:

$$J(\theta) = \mathbb{E}\left[\sum_{k=0}^{h} \frac{r(k)}{h}\right],$$

where $r(k, x(k), u(k)) \in \mathbb{R}$ is the reward at the current time step, k, $x(k) \in \mathbb{R}^q$ is the current state, $u(k) \in \mathbb{R}^r$ is the current action, and h is the time horizon. The state can evolve stochastically according to $x(k+1) \sim p(x(k+1) \mid x(k), u(k))$, while the action depends on the parametrized policy, π_θ, such that $u(k) \sim \pi_\theta(u(k) \mid x(k))$. The sequence of states and actions forms a trajectory denoted by $\tau = [x(0:h), u(0:h)]$. The policy parametrization is updated according to the gradient update rule:

$$\Delta\theta_s = \alpha_s \nabla_\theta \left. J \right|_{\theta=\theta_s},$$

where $\alpha_s \in \mathbb{R}_+$ denotes the learning rate and $s \in \mathbb{N}_0$ is the current update number.

The policy gradient algorithm we use is a finite-difference method, which varies the policy parametrization by small increments $\Delta\theta_s$ and generates an estimate of the expected return $\Delta\hat{J}_s \approx J(\theta_s) - J(\theta_s - \Delta\theta_s)$ based on a backward-difference estimator. It then computes the policy gradient estimate using regression:

$$\nabla_\theta \left. J \right|_{\theta=\theta_s} \approx \left(\Delta\Theta^T \Delta\Theta\right)^{-1} \Delta\Theta^T \Delta\hat{J},$$

where $\Delta\Theta = [\Delta\theta_{k-1}, \Delta\theta_k]^T$ and $\Delta\hat{J} = \left[\Delta\hat{J}_{k-1}, \Delta\hat{J}_k\right]^T$. The algorithm then repeats until $\Delta\theta_s$ is smaller than a predetermined threshold.

We choose the scale-dependent root mean square error between the integrated optical flow signals and their gyroscope counterparts as our reward:

$$r_u(k) = -\sqrt{\mathbb{E}\left[(u_{int} - \omega_z)^2\right]},$$
$$r_v(k) = -\sqrt{\mathbb{E}\left[(v_{int} - \omega_y)^2\right]}.$$

Note that the optical flow signals are first linearly interpolated to the timestamps of the gyroscope signal, given its much higher sampling frequency.

Using a learning rate of $\alpha = 1$ and a policy parameter threshold of $\Delta\theta_s < 10^{-5}$, we ran the reinforcement learning algorithm to estimate the scaling parameter in $n = 9$ experiments as presented in the previous section. We then computed the mean and standard deviation of the results, included as part of Table 3.1, which when applied to the data plotted in Figure 3.4 results in Figure 3.5. Note how closely the optical flow estimates, u_{int} and v_{int}, follow the corresponding gyroscope signals.

For each scaling parameter, Table 3.1 includes three columns of root mean square error (RMSE) values. The first one corresponds to the original RMSE when no scaling is applied to the signals. The second one is the RMSE when scaled with the learned scaling factor for that particular experiment, s_u and s_v, and the third is the RMSE when scaled with the mean scaling parameter, μ_u and μ_v.

n	s_u	RMSE			s_v	RMSE		
1	30.35	12.00	0.58	1.14	80.75	15.39	0.70	0.98
2	11.06	4.60	0.44	0.46	147.13	64.75	0.72	3.33
3	9.30	3.47	0.50	0.50	161.33	67.42	0.71	3.50
4	8.07	2.91	0.50	0.50	134.00	54.73	0.69	2.80
5	9.04	3.25	0.47	0.47	126.65	53.43	0.68	2.71
6	5.10	2.41	0.45	0.52	86.90	52.26	0.71	2.49
7	19.75	7.33	0.51	0.69	81.83	39.79	0.64	1.90
8	21.55	9.23	0.61	0.88	35.01	19.67	0.68	0.88
9	7.38	3.79	0.97	0.98	22.39	13.60	0.94	0.96
μ	13.51 ± 7.95	1	s_u	μ_u	97.33 ± 45.83	1	s_v	μ_v

Table 3.1: Learned scaling parameters. The three RMSE columns correspond to the errors for the original signal, the signal scaled by the scaling parameter learned for that experiment, and the signal scaled by the mean scaling parameter.

Because of the large standard deviations portrayed in Table 3.1, we do not expect that just applying the mean scaling factor, as done in Figure 3.5, will necessarilly result in the optical flow estimates perfectly representing the relevant physical quantities (i.e. radians per second).

3.5 Concluding remarks

In this chapter we characterized our sensing board and the algorithms that are run on the captured signals. We identified a scale ambiguity between the optical flow estimates and the corresponding gyroscope readings and applied the finite- difference policy gradient reinforcement learning optimization algorithm to find the scaling factors for each axis, which was applied to experimental data with positive results. Yet, the standardized scaling factors may not perfectly recover the correct rotational rates for all experiments.

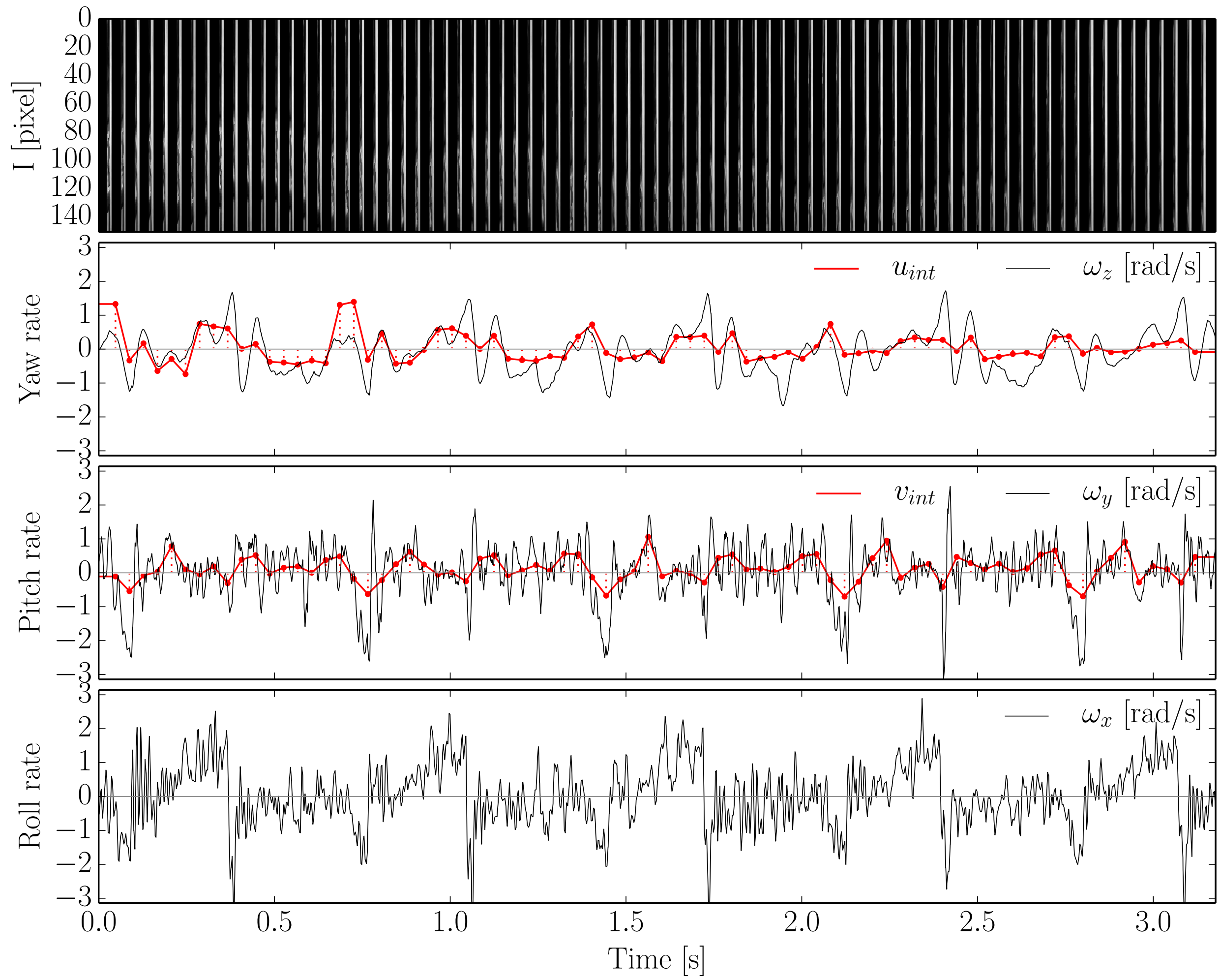

Figure 3.5: Optical flow estimates with applied scaling factor versus gyroscope readings for the same experiment as in Figure 3.4. Notice the correlation between the yaw and pitch optical flow estimates, u_{int} and v_{int}, and the corresponding gyroscope signals.

Chapter 4

Disambiguate unsteady optical flow

In this chapter, we compare the optical flow signals obtained during a looming experiment using both a steady and an unsteady platform. Since the unsteadiness usually overwhelms the optical flow estimates, we propose image derotation as a method to disambiguate the estimates by leveraging the gyroscope sensor. We then introduce a 2D and a 3D simulation of the experiment to validate the derotation procedure in a controllable environment.

4.1 Locomotion platforms and experimental setup

To more clearly understand the distinction between steady and unsteady locomotion and how it affects optical flow estimation, we used two distinct platforms: a camera dolly[1] and the VelociRoACH robot (Haldane et al. 2013) with an added camera at the front (see Figure 4.1). Both platforms carry the same embedded sensing hardware (Baek, Garcia Bermudez, and Fearing 2011) that includes a VGA camera, an inertial measurement unit, and an 802.15.4 wireless radio for issuing control commands and downloading telemetry data[2].

The experimental arena portrayed in Figure 4.1a has a laminate tile floor, a checkerboard pattern on one side, and unconstrained views of the laboratory on the other sides. Ground truth data is collected using an OptiTrack[3] motion capture system comprised of eight V100:R2 cameras located .45 m above the terrain and capable of sub-millimeter accuracy as specified by the manufacturer. This arena is used for both the looming and the translation experiments.

The looming experiment consists of having the platforms approach the checkerboard-patterned side starting .3–.5 m away from it, while the translation experiment consists of having them move towards any of the uncovered sides, where the laboratory background is 3–5 m away. Due to the order of magnitude difference in the distance to the objects that the robots are approaching, the corresponding looming signals, as estimated from the

[1] Revolve Camera Dolly: http://www.revolvecamera.com/
[2] Embedded board: https://github.com/biomimetics/imageproc_pcb
[3] NaturalPoint, Inc. OptiTrack: http://www.naturalpoint.com/optitrack/

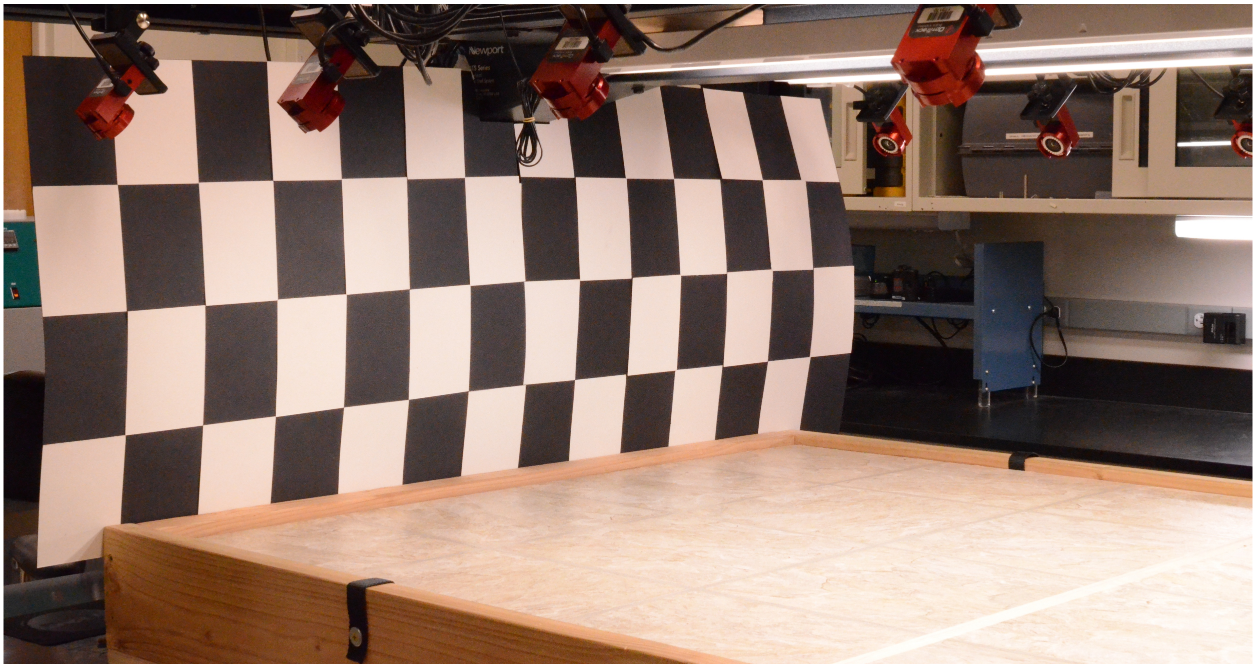

(a) Experimental arena

(b) Revolve camera dolly

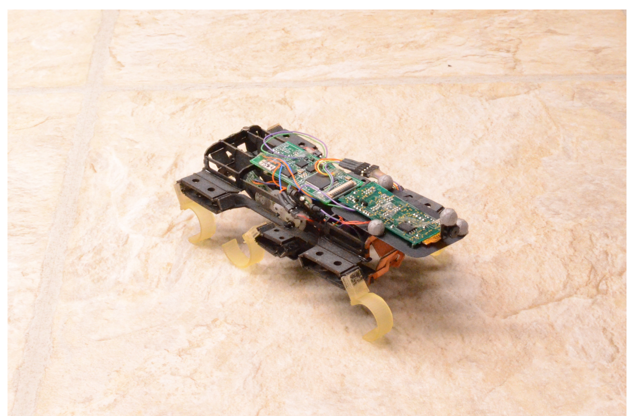

(c) VelociRoACH legged robot

Figure 4.1: The (a) experimental arena with a floor of laminate tile, a side covered in a checkerboard pattern, three other sides with unconstrained views of the laboratory, and an OptiTrack system for recording ground thruth motion capture data. The platforms used to investigate (b) steady locomotion and (c) unsteady locomotion carry the same embedded electronics package, which includes a camera, an inertial measurement unit, and an 802.15.4 wireless radio among its features.

optical flow, will be much larger in the looming experiment than in the translation one. The background texture for the looming experiment also has starker contrast, due to the coarse checkerboard pattern, which results in stronger optical flow signals at the edges.

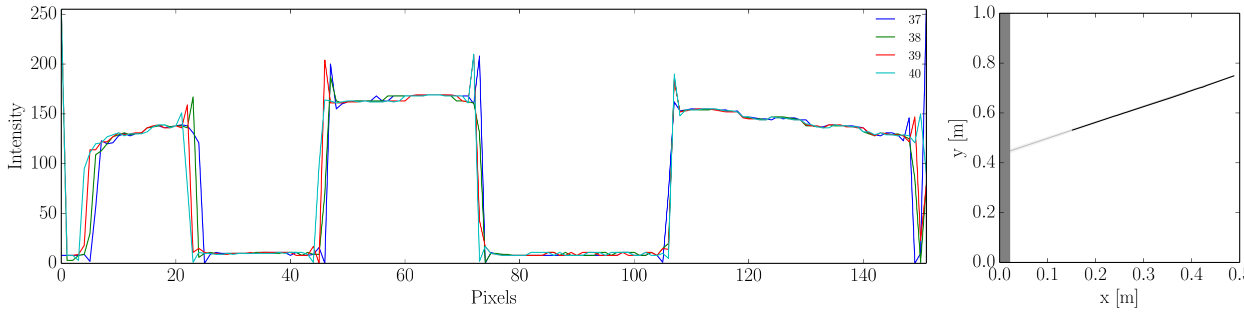

(a) Camera dolly

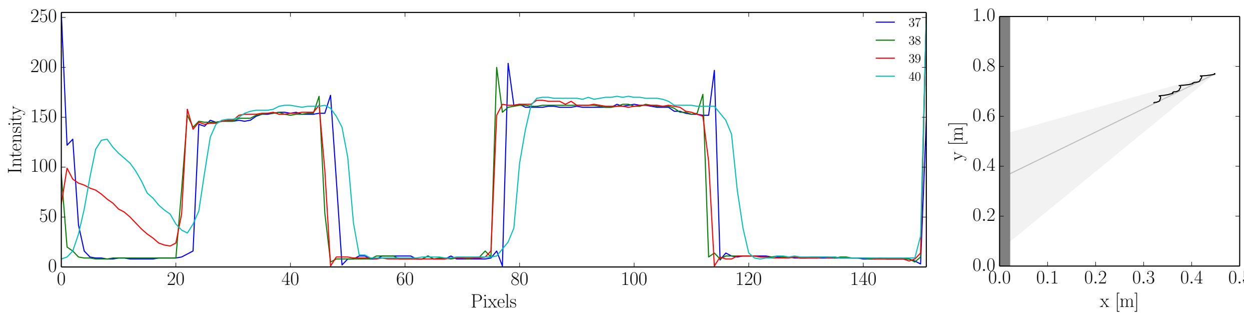

(b) VelociRoACH

Figure 4.2: Intensity values of row 10 for frames 37–40 in looming experiments on-board the (a) steady and (b) unsteady platforms. The corresponding x-y trajectories towards the checkerboard pattern have an overlaid estimate of the locomotion direction and a one standard deviation confidence interval.

4.2 Looming experiment from the perspective of a single image row over time

So as to clearly visualize the raw image intensities in time, we'll first focus our analysis on a single row per frame. The bottom half of experimental frames usually includes some portion of the rather featureless floor, so we pick row 10 on the top half of each frame to ensure that it represents a part of the checkerboard pattern. For more details on the sampling characteristics, please refer to Section 3.2.

Figure 4.2 shows plots of the intensity values for four consecutive rows in the middle of an experimental run (frames 37–40) for the camera dolly and the VelociRoACH platforms. It also shows the x-y trajectory that each of these platforms traversed as they approached the checkerboard pattern with an overlaid estimate of the locomotion direction and a one standard deviation confidence interval.

As expected, the camera dolly experiment produces smoother motions of the camera as it approaches the checkerboard pattern. Around pixels 21–24, for example, there is an edge that moves towards the left at a rate of about 1 pixel/frame. The VelociRoACH experiment, on the other hand, presents oscillatory motions that are clearly visible in the direction plot. Even on relatively clear edges, like the one around pixels 75–80, one can see the edge

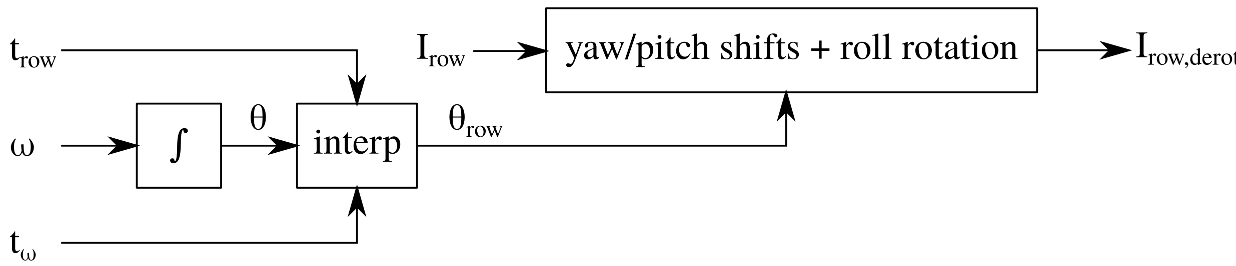

Figure 4.3: Block diagram of the image derotation algorithm.

oscillating with rather large amplitudes as the robot slowly locomotes forward. This poses a series of problems for our analysis. Not only will the looming data be mixed with the unsteady nature of legged locomotion, but the large amplitude motions of the edges that move at rates upward of 1 pixel/frame would result in innacurate motion estimates.

4.3 Gyroscope-based image derotation

Section 3.4 underscored how closely the optical flow estimates in the yaw and pitch directions follow the robot's oscillations. In this section, we introduce a method of filtering out these oscillations by fusing the gyroscope measurements with the image data. This allows us to more readily extract exteroception information from the optical flow estimates and because the derotation is performed at the row level, it should also help alleviate the camera's rolling shutter effect.

Given that the gyroscope is sampled at a frequency of 1 KHz alongside the image rows and that both sampling events are timed to microsecond accuracy, one can interpolate the gyroscope measurements in order to derotate each image row. We derotate in yaw, by shifting the rows horizontally, in pitch, by shifting the rows vertically, and in roll, by rotating the whole image and resampling the relevant row. This derotation is applied for each row in three steps. The first step performs the yaw and pitch shifts measured for that row on the full frame while the second step rotates the shifted frame using the roll measurement for that row. The final step resamples the relevant row from the shifted and rotated frame. Because rotations are not necessarilly commutative, this order can introduce a bias. Derotation is simplified by the fact that the set of axes for the gyroscope and camera match, as shown in Figure 3.3, and that the image axes (u and v) also follow the same sign convention as the corresponding camera axes (yaw and pitch). Figure 4.3 displays the block diagram for this algorithm.

Applying image derotation to the VelociRoACH experiment introduced in Figure 4.2b results in the following set of figures that detail the algorithm's effect when derotating one axis at a time or all axes at the same time. In particular, the derotation effect in yaw is shown in Figure 4.4, in pitch in Figure 4.5, in roll in Figure 4.6, and in all axes in Figure 4.7. For each figure, the top plots illustrate how the original frames, 37–40, get derotated based

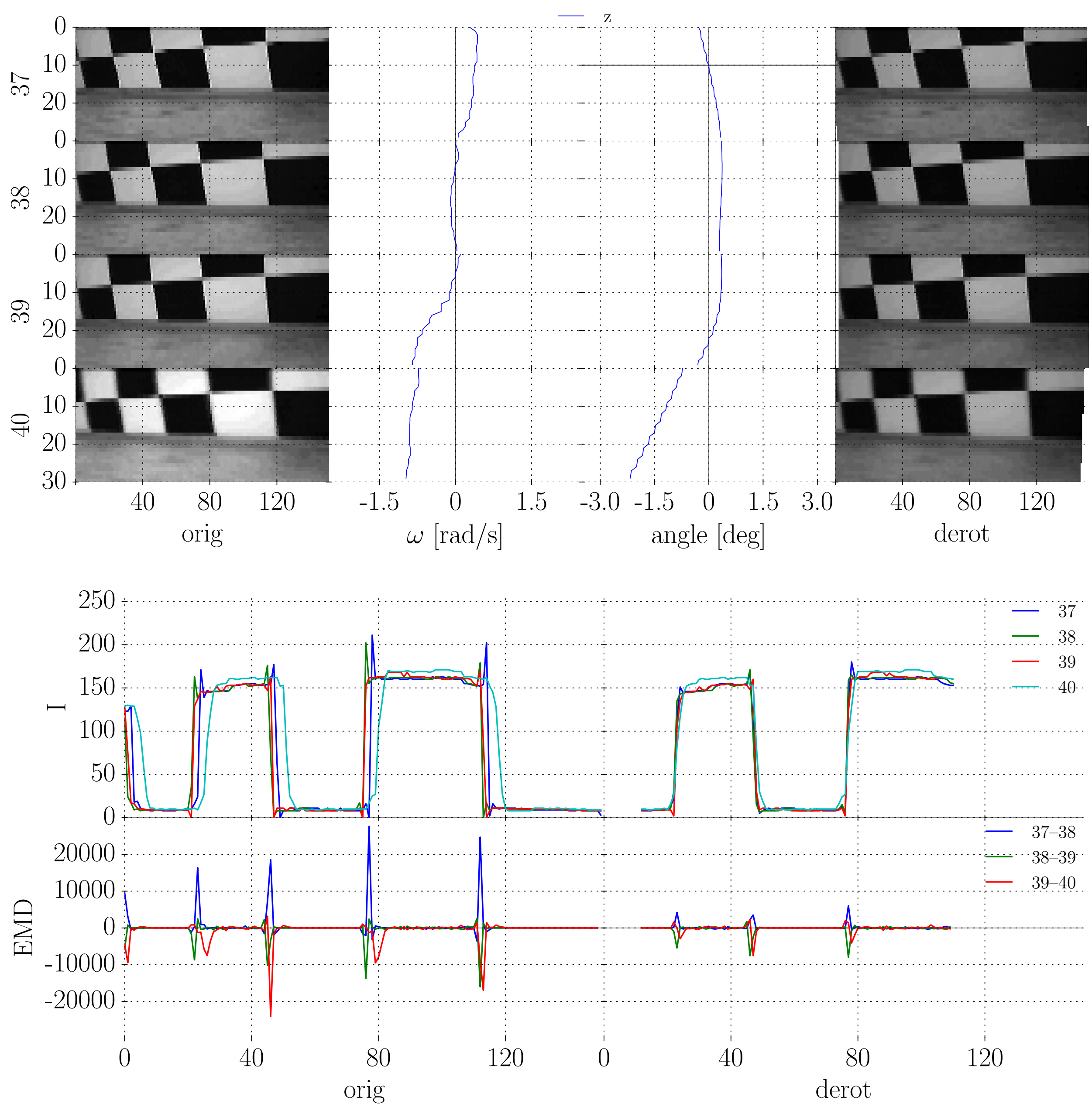

Figure 4.4: Effect of yaw derotation for the VelociRoACH experiment introduced in Figure 4.2b. The top plots illustrate how the original frames, 37–40, get derotated based on the gyroscope and corresponding angle signals. For easier comparison, we shift the angle signal's baseline so there's a zero crossing at row 10 of the first frame. The bottom plots show the intensity values for this same row before and after derotation along with the corresponding optical flow output, which is computed using frame n and $n + 1$.

on the gyroscope and corresponding angle signals. For easier comparison, we shift the angle signal's baseline so there's a zero crossing at row 10 of the first frame. The bottom plots of each figure show the intensity values for this same row before and after derotation along

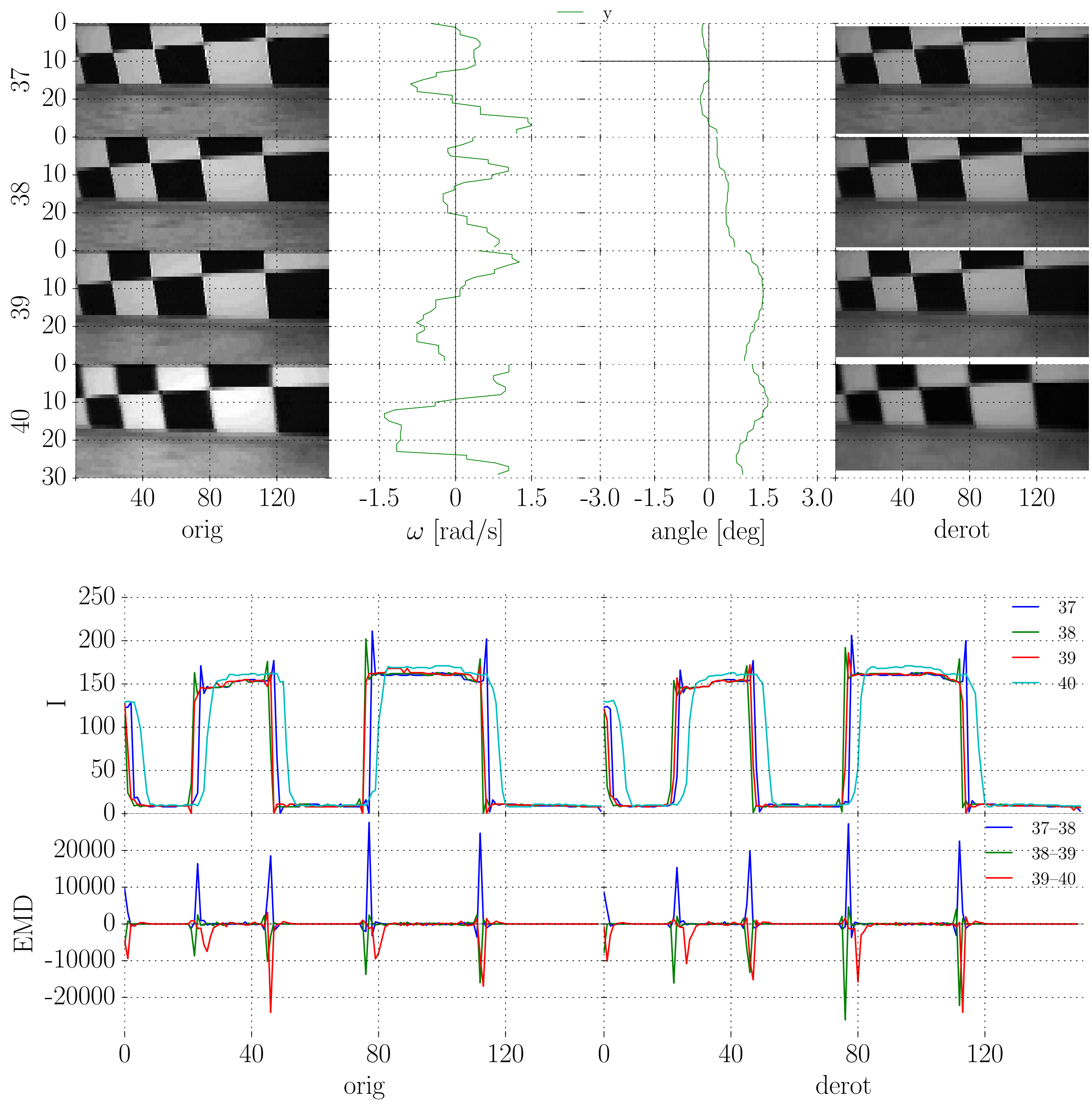

Figure 4.5: Effect of pitch derotation for the VelociRoACH experiment introduced in Figure 4.2b. See Figure 4.4 for more details on the signals plotted. Note that even though frames are significantly raised or lowered, its effect on the optical flow output for the row is comparatively small, since the motion compensated for is perpendicular to that estimated across the row's pixels.

with the corresponding optical flow output, which is computed using frame n and $n+1$.

One thing to note is the discontinuity of the gyroscope and angle signals between frames. We are only plotting the portion of these signals that was captured concurrently with the image information and leaving out the data captured when no frames were being output.

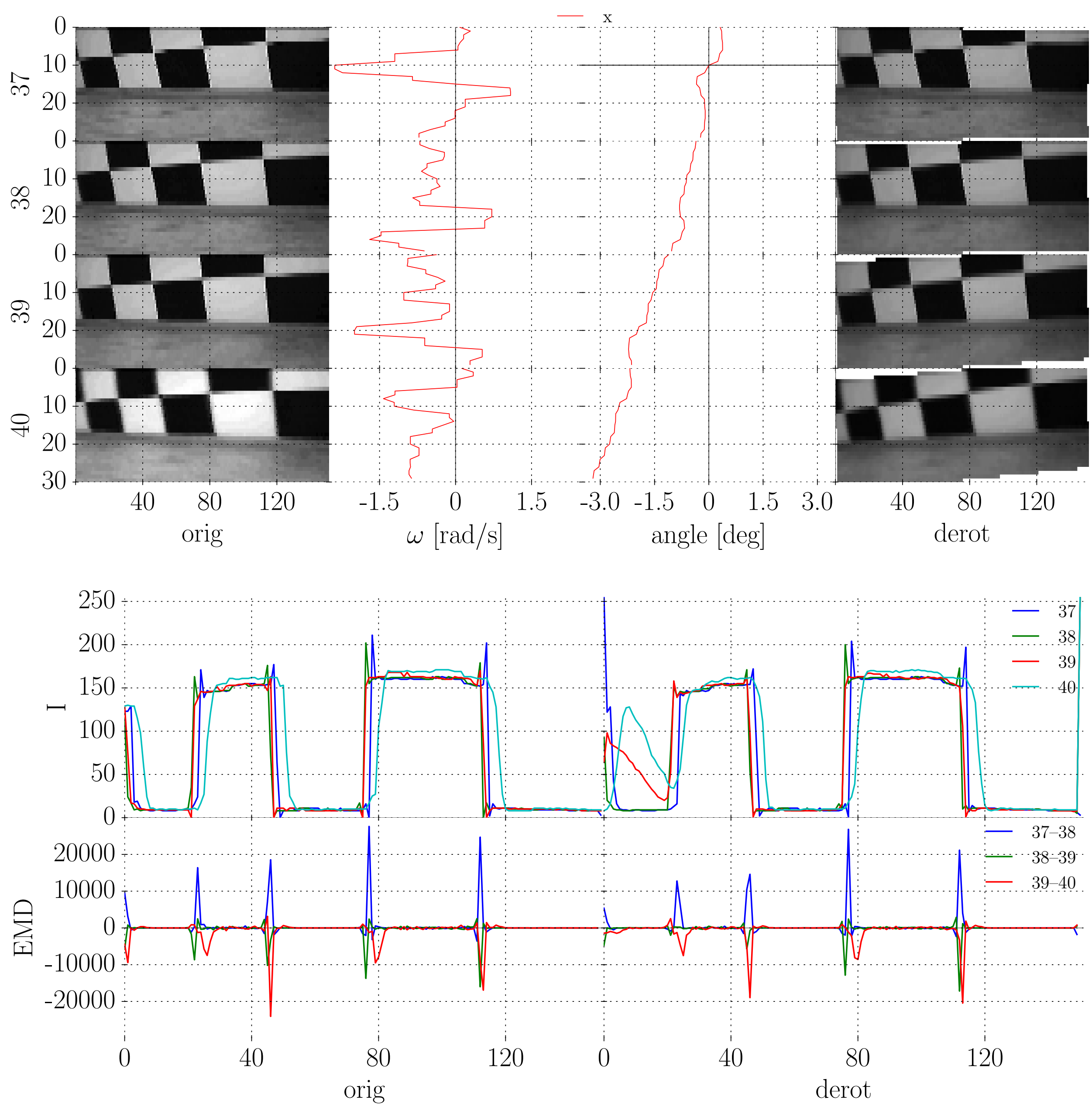

Figure 4.6: Effect of roll derotation for the VelociRoACH experiment introduced in Figure 4.2b. See Figure 4.4 for more details on the signals plotted. Note that the derotated frames are a bit misleading at portraying the derotation angle because they're not plotted at the correct aspect ratio.

Please refer to Section 3.2 for further information on the sensors' sampling characteristics.

The derotation axes with the most noticeable effect on the optical flow estimates of row 10 are yaw, which acts longitudinally across the row (see Figure 4.4), and roll, which affects the longitudinal information significantly, particularly if it does not properly derotate the robot's motion (see Figure 4.6). Gyroscope measurements usually drift over time and this

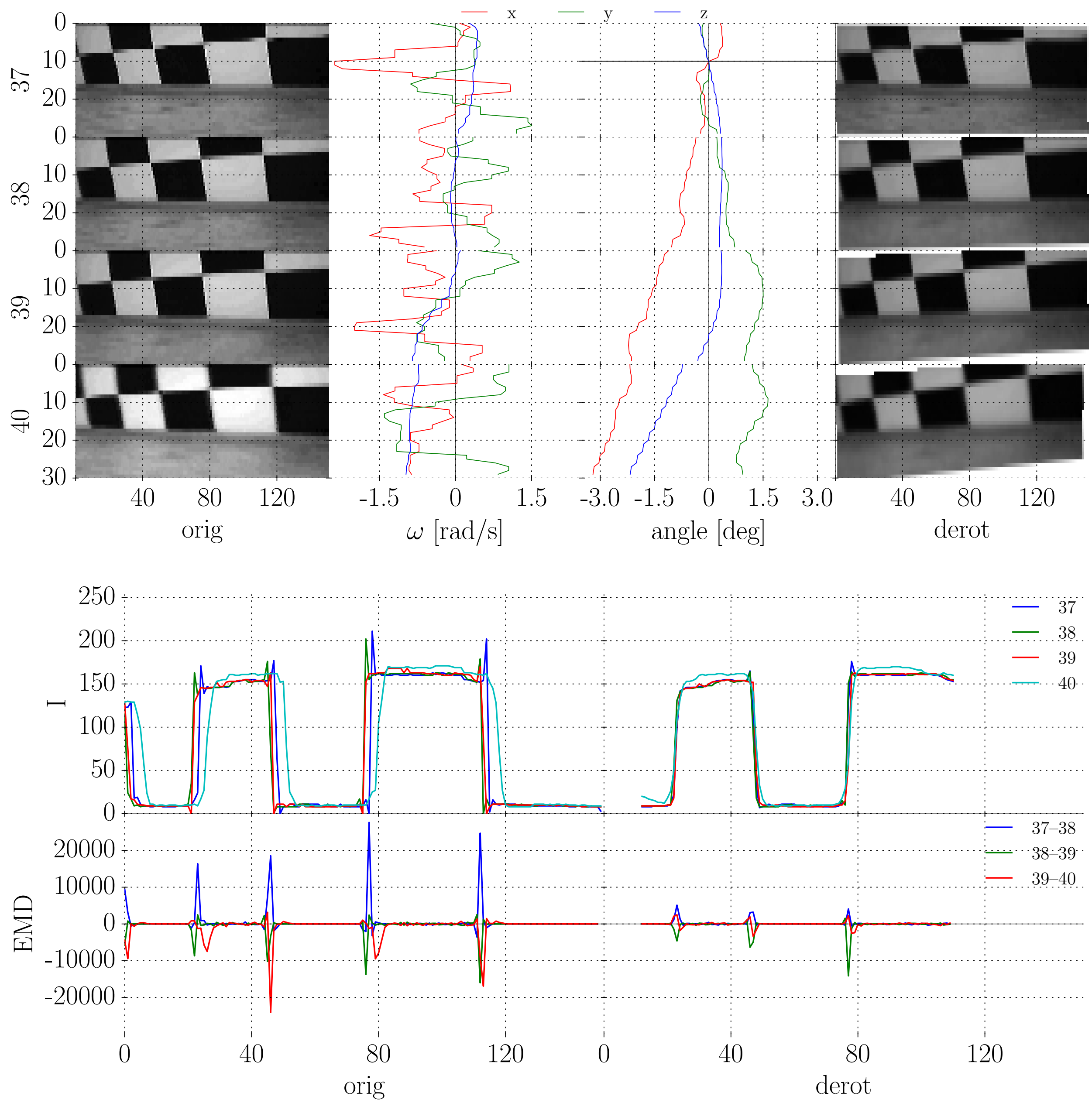

Figure 4.7: Derotation effect for the VelociRoACH experiment introduced in Figure 4.2b. See Figure 4.4 for more details on the signals plotted. Note how the derotation's algorithm overcompensates for the robot's motion, partly due to gyroscope measurement's drift, which accumulates in the angle signal.

can turn out to be significant when integrating the signal. This is partly the reason why our algorithm overcompensates for the robot's motions, which can be observed in the roll derotation plots.

Also note that the roll derotation has not been able to fully reduce the disparity between the edges. As an example, the edge at pixel 50 jumps 4–5 pixels from frame 39 to 40.

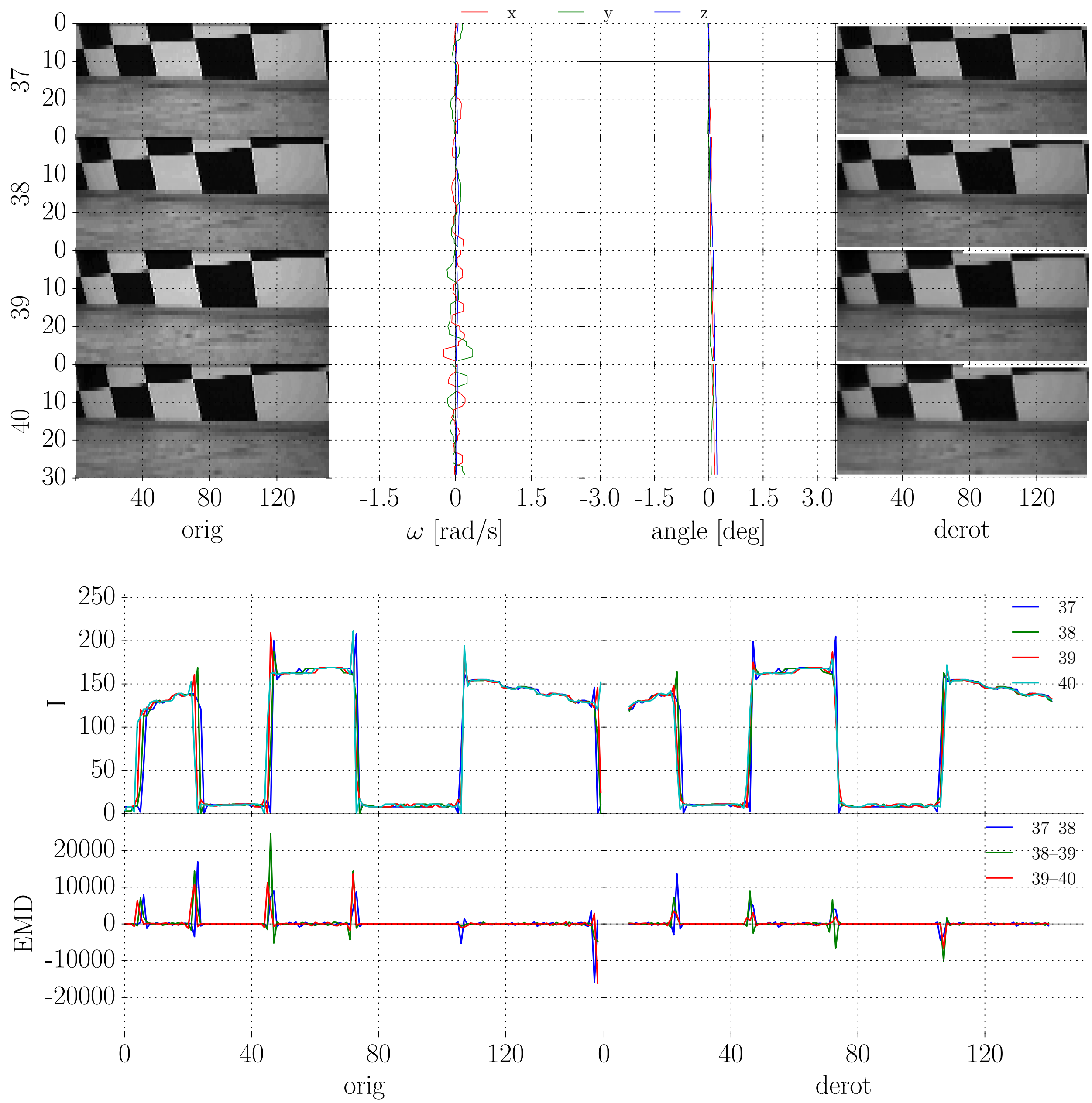

Figure 4.8: Derotation effect for the camera dolly experiment introduced in Figure 4.2a. See Figure 4.4 for more details on the signals plotted. We don't expect large oscillations in this experiment, particularly given the linear direction plot of Figure 4.2a. The angle signal should thus be a good measure of gyroscope drift, although it might also encode an arced or uneven locomotion surface.

The optical flow output would not be accurate in this case either before or after derotation, because it's based on just comparing neighboring pixels. Thus, given the horizontal pixel's field of view of .005192 rad and a 25 Hz framerate, the maximum rotational rate the algorithm could estimate by just comparing two neighboring pixels is 7.437 deg/s. We don't pursue it in this work, but a way to increase this estimation limit is to apply a Gaussian pyramid to the input data, which with just one step would double the estimation limit.

The compound derotation shown in Figure 4.7 illustrates how, even if the derotation algorithm is trying to fully account for the robot's motion, it does not fully recover a clean looming signal. Nonetheless, it does help reduce the overall effect of the robot's locomotive unsteadiness by reducing the optical flow's output amplitude and on average approaches the looming result attained by the steadier platform, which we observe next.

Figure 4.8 shows the effect of the derotation algorithm on the camera dolly experiment first introduced in Figure 4.2a. We do not expect large oscillations for the camera dolly as we do for the VelociRoACH, but we still see small oscillations throughout. The laminate tile surface is not perfectly flat and there are potential bumps when crossing tiles. The overall surface might also be slightly arced over long stretches. This, alongside the usual gyroscope drift, could contribute to the slowly increasing angle signal. Its effect on the optical flow estimates after derotation is minimal when compared to the VelociRoACH experiment, but derotation does help clean up the optical flow output, particularly by taking care of its larger peaks.

4.4 Translation experiment on the VelociRoACH

In order to understand how the unsteady dynamics of the VelociRoACH robot affect optical flow estimation, we first perform a translation experiment where the robot locomotes across the arena while observing the laboratory background at a distance. The absence of strong looming signals, based on the distance to the background and the weaker contrast it offers, results in optical flow estimates that are mostly driven by the robot's unsteady dynamics.

Figure 4.9 shows the output of a translation experiment on-board the VelociRoACH. The top plot displays the on-board video sequence as the robot locomotes on the arena. Note how the laboratory background has weaker contrast than the checkerboard pattern that can be seen in Figure 4.13. The other three plots display the rotational rates as measured by the gyroscope and estimated by the optical flow algorithm in yaw, pitch, and roll.

The yaw rotational rate estimated by the optical flow algorithm, u_{int}, is well correlated with its gyroscope counterpart ($\rho_u = .58$), while the pitch rotational rate, v_{int}, is less so ($\rho_v = .26$). This can be readily explained by the sampling characteristics in each dimension. Whereas 152 pixels are captured for each row (out of a maximum of 160 pixels), only 30 pixels are captured for each column (given that only 1 every 4 rows are captured, out of a maximum of 120). Thus, even though the pitch optical flow estimates carry useful information, we won't rely on them heavily given the high likelihood of spatial aliasing.

The result of applying derotation to this VelociRoACH translation experiment can be visualized in Figure 4.10. Note, in particular, how the derotation's effect is visible in the top plot, where the video sequence's texture, previously oscillating along with the robot, is now much steadier. Yet, the derotation's effect is not perfect, and the unsteadiness left is enough to generate oscillatory optical flow, which is particularly visible in the yaw rate plot.

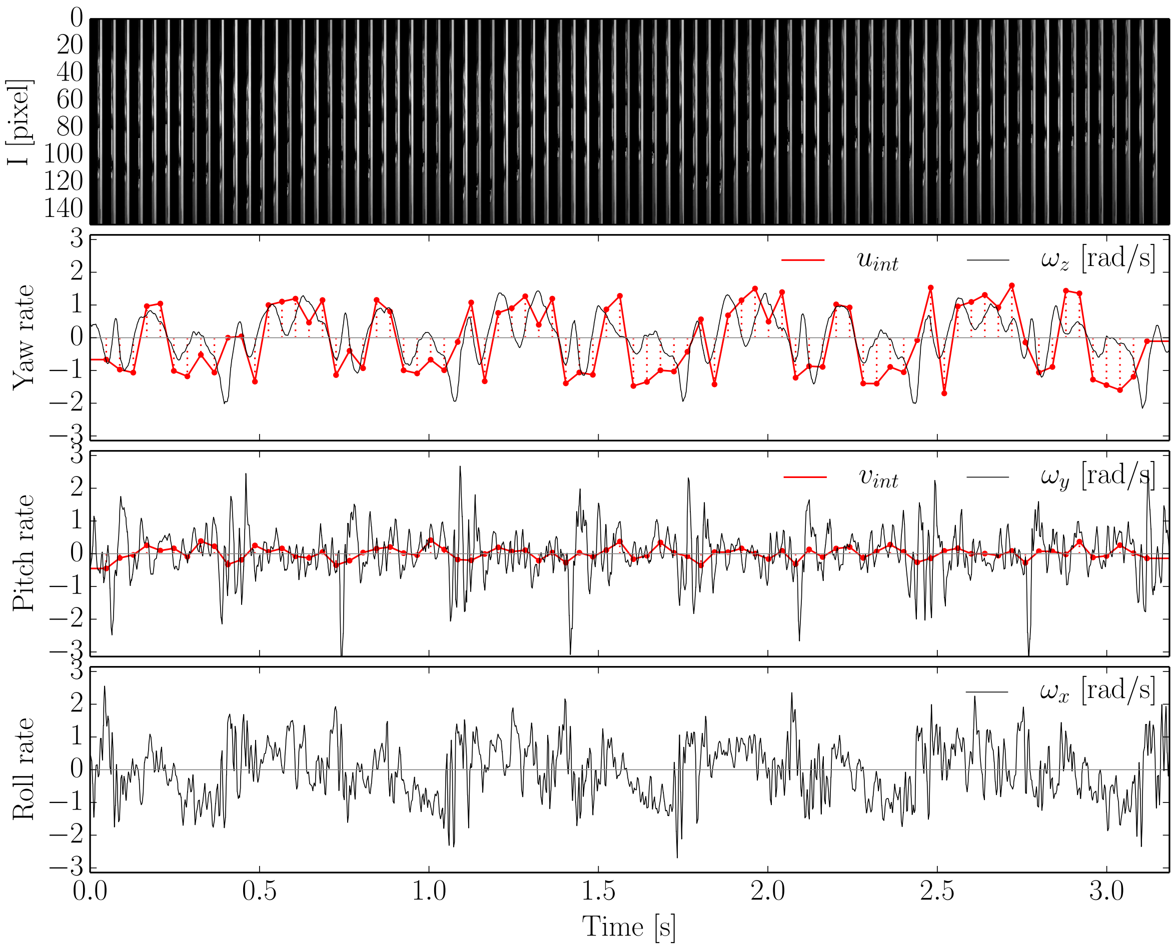

Figure 4.9: Translation experiment on the VelociRoACH robot. The top plot displays the on-board video in time as the robot locomotes across the arena. Note the weaker texture of the laboratory background compared to the checkerboard pattern present in Figure 4.13. The other three plots display the gyroscope and the integrated optical flow estimates in yaw, pitch, and roll. The yaw optical flow estimates, u_{int}, are well correlated to the gyroscope measurements while the pitch estimates, v_{int}, are less so. This is probably due to sparse sampling of columns (only 1 every 4 pixels are kept) while each row is almost entirely captured. Thus, even though the pitch optical flow estimates carry useful information, we won't rely on them heavily given the high likelihood of spatial aliasing.

Still, the amplitude of the resulting optical flow signal is quite reduced when compared to the original estimates.

In order to better examine the performance of the derotation algorithm, we introduce a 2D simulation of an oscillating camera with similar characteristics to the one we use on-board the robot. The camera images a single object in the environment, which is represented by a 10 cm × 10 cm white bar that is 50 cm away from it and has an intensity of 255 (pure white) against a background instensity of 0 (pure black). Each camera pixel has a field of view of .005192 rad × .004765 rad. The camera oscillates in yaw with a sinusoidal motion of 3 Hz and unitary amplitude. The output of this simulation is displayed in Figure 4.11. As expected, the optical flow algorithm correctly tracks the camera motion in this simplified

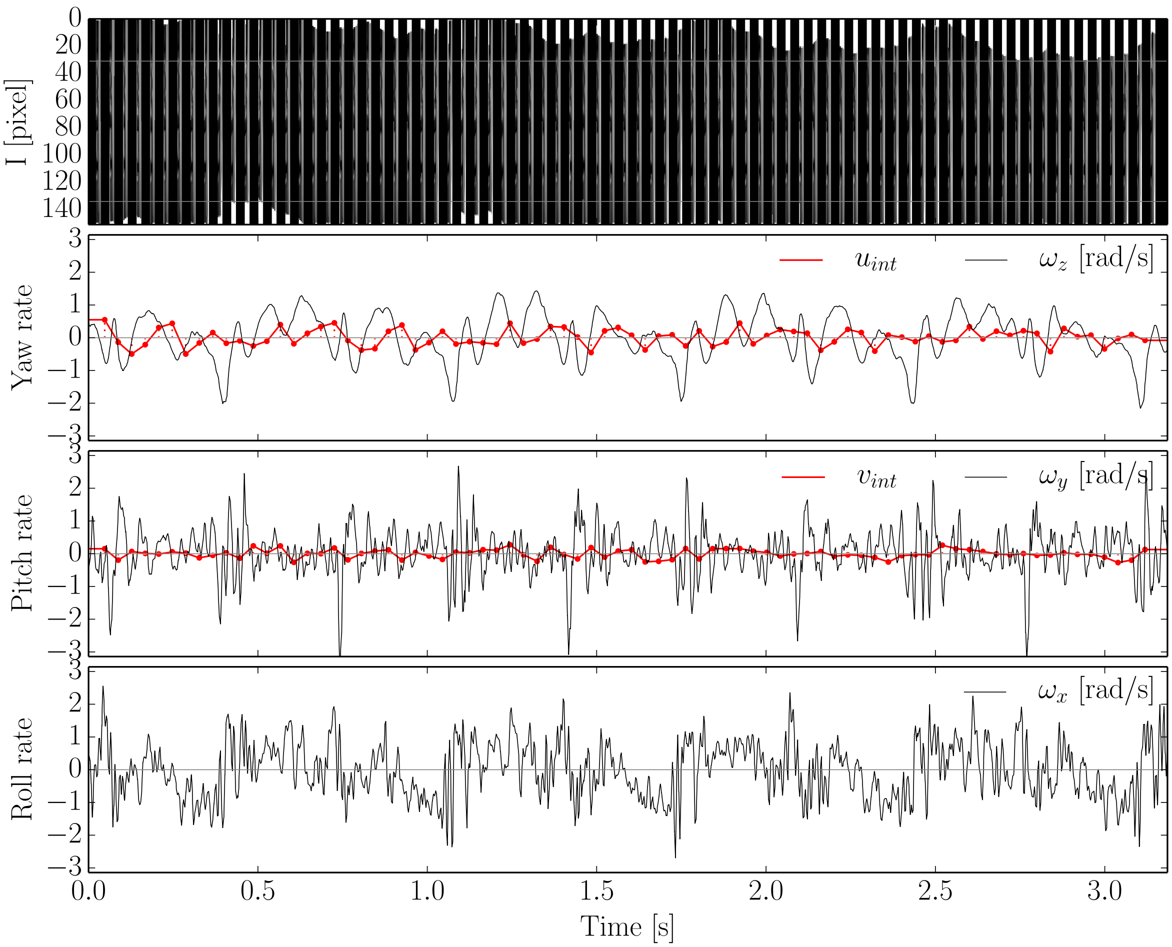

Figure 4.10: Translation experiment on the VelociRoACH robot after derotation. Note how the previously oscillating texture shown in the top plot is steadier throughout the video sequence. The derotation is far from perfect, though, and the unsteadiness left in the video sequence is enough to generate oscillatory optical flow, particularly visible in the yaw plot, but its amplitude is quite reduced. For a detailed description of what each plot displays, please refer to Figure 4.9.

case, generating a strong signal in the yaw direction.

Applying the derotation algorithm to this simplified case fully recovers a steady video sequence of the bar, which results in null optical flow in the yaw direction, as can be observed in Figure 4.12. Note how the optical flow signal in the pitch direction is slightly nonzero throughout the simulation output before and after the derotation. This is an artifact generated by the interpolated edges of the bar as they are shifted by sub-pixel amounts due to the coarse resolution of each video frame (152 pixels $\times$ 30 pixels).

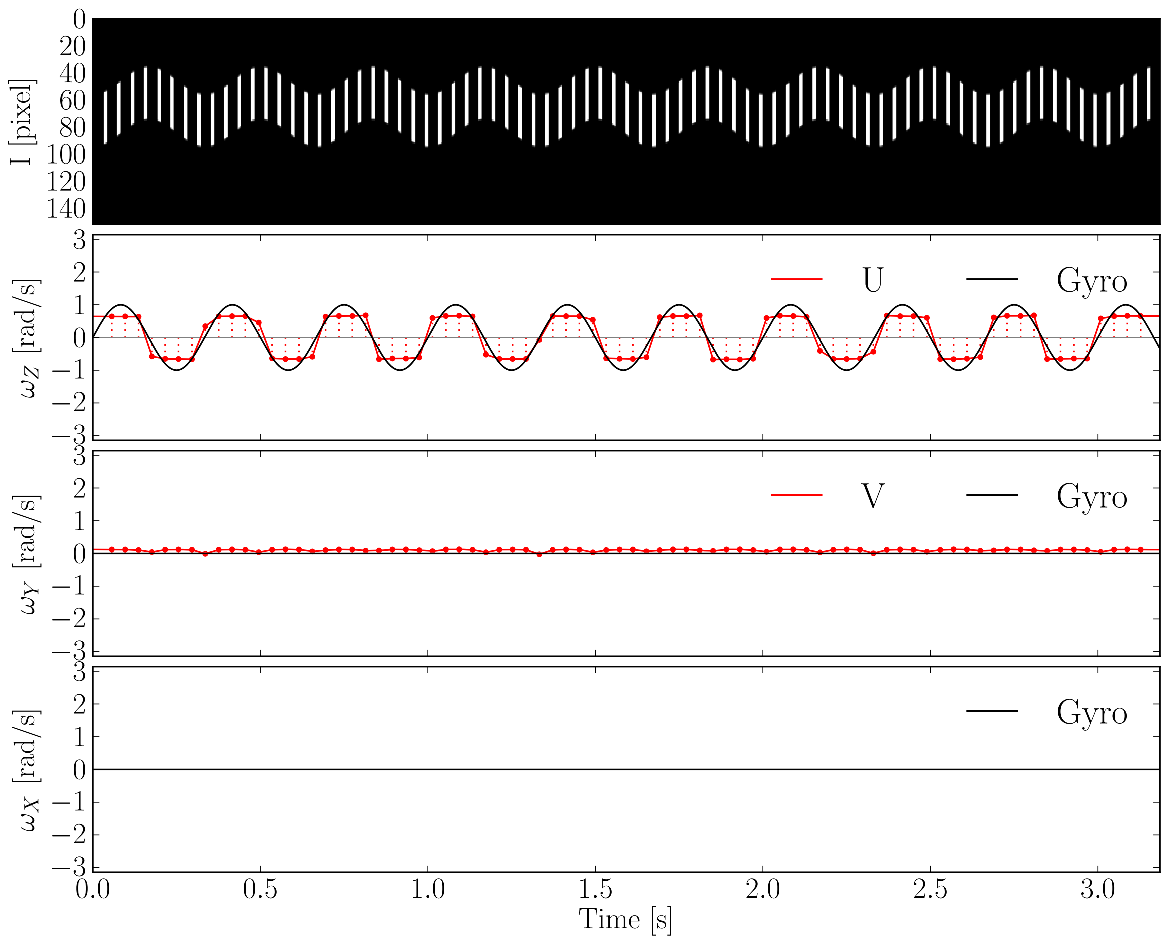

Figure 4.11: Simulation of an oscillating camera in yaw. The camera oscillates with sinusoidal motion in front of a white bar and this elicits a strong optical flow signal in yaw that tracks the camera motion. For a detailed description of what each plot displays, please refer to Figure 4.9.

4.5 Looming experiment on the camera dolly

The looming experiment on the camera dolly consists on the dolly approaching the checkerboard pattern at an angle of about 30 deg to the right of the center of the checkerboard (this can be observed in the direction plot in Figure 4.2a). Because of this, we expect the looming signal to be assymetric about the center of the optical flow field. Figure 4.13 shows the looming output of the camera dolly experiment introduced in Figure 4.2a.

The top plot in Figure 4.13 displays the video sequence captured on-board as the dolly approached the wall. Note how the black and white stripes of the checkerboard increase in size as the camera gets closer to the pattern. Also notice how there is an assymetry in this expansion when you compare the top portion of the video sequence (left side of the dolly) with the bottom portion of it (right side of the dolly). The bottom portion shows expansion of a black stripe, which marks an approximate focus of expansion for the optical flow field

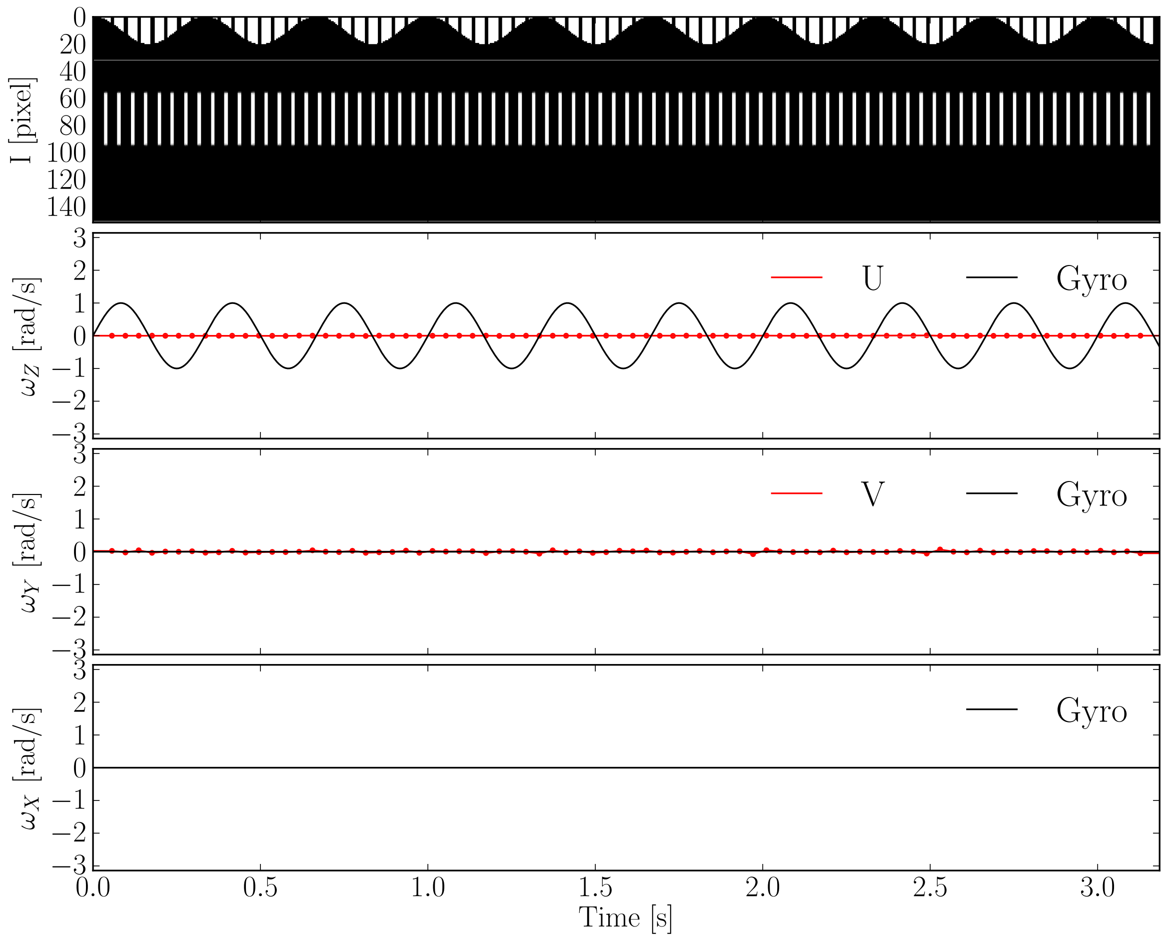

Figure 4.12: Simulation of an oscillating camera in yaw after derotation. Given the full knowledge of the generating signal, which is a perfect oscillation in yaw, the derotation algorithm is able to fully recover a steady video sequence of the bar. This results in a zero optical flow signal in yaw, as expected. For a detailed description of what each plot displays, please refer to Figure 4.9.

and thus the direction of motion of the robot as it approaches the pattern.

The bottom plot in Figure 4.13 displays the yaw rotational rates as measured by the gyroscope and estimated by the optical flow computation. It thus compares the optical flow in the yaw direction integrated across the whole field with the yaw gyroscope measurement. Whereas the gyroscope shows that there's almost no yaw oscillations as the dolly approaches the wall, the optical flow output represents the looming information that the checkerboard's texture generates as its edges rotate out of the field of view. This bottom plot also includes the optical flow estimates integrated across the left and right halves of the field of view, which show that the largest motion estimates occur on the left half of the flow field not only due to the faster motion on that side, but also due to the greater number of edges in that section.

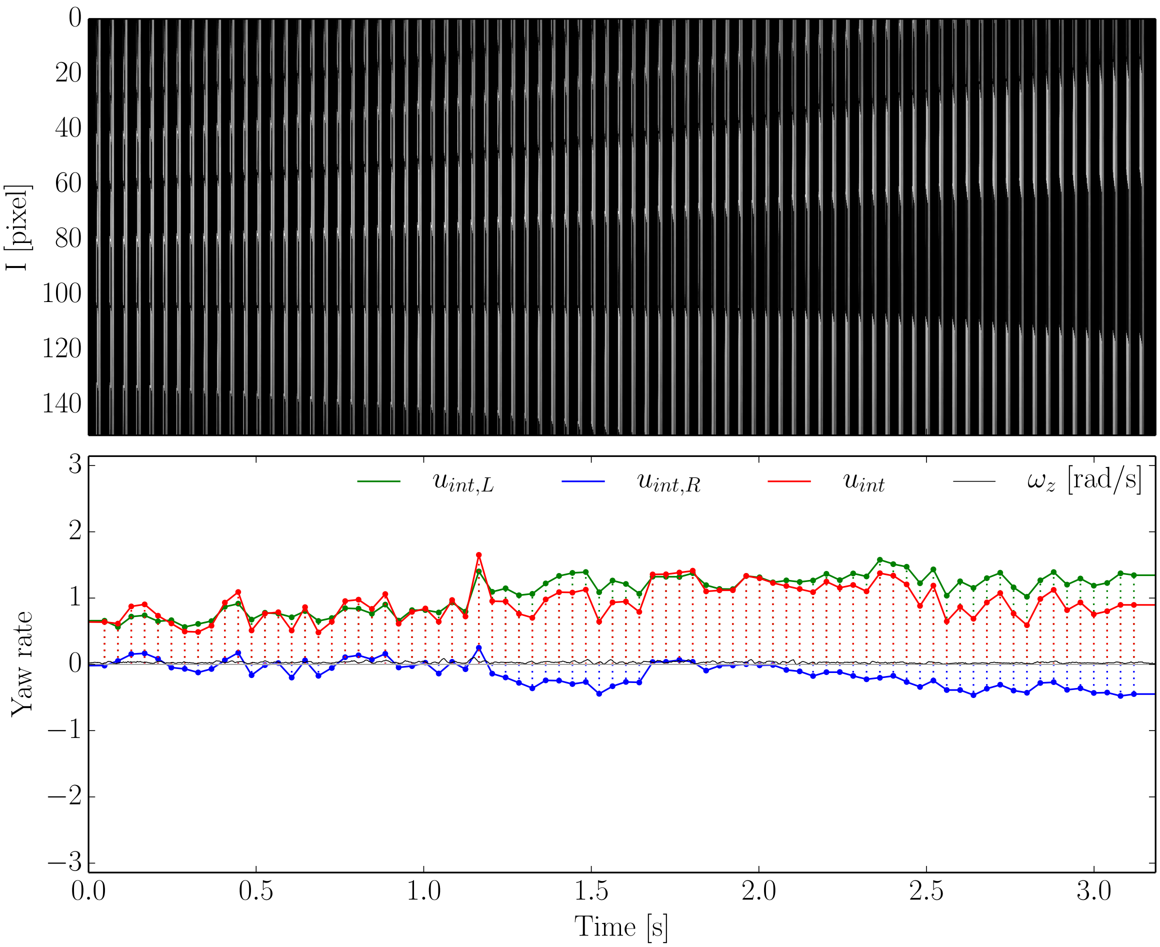

Figure 4.13: Looming experiment on the camera dolly experiment introduced in Figure 4.2a. The video sequence captured by the on-board camera is plotted in time at the top, while the yaw rotational rates as measured by the gyroscope and the optical flow algorithm are plottled at the bottom. The bottom plot also compares the integrated optical flow output as computed across the whole optical flow field with that computed across just the left and right sides of this same field so as to visualize the assymetry of the looming information.

Figure 4.14 shows the looming information for a 3D simulation produced in Blender[4] of the experiment plotted in Figure 4.13. The simulation starts from the same starting point as the experiment, in a simulated 3D reconstruction of the experimental arena, and locomotes towards the checkerboard pattern at the experiment's average angle of approach and velocity. Lighting in the simulation is not exactly the same as that in the experiment so the contrast of the checkerboard pattern is starker, resulting in larger optical flow estimates. Disregarding the scaling differences for the moment, the overall looming results are consistent between both experiments, showing increased output on the left side of the optical flow field.

[4]Blender 3D Content Creation Suite: http://www.blender.org/

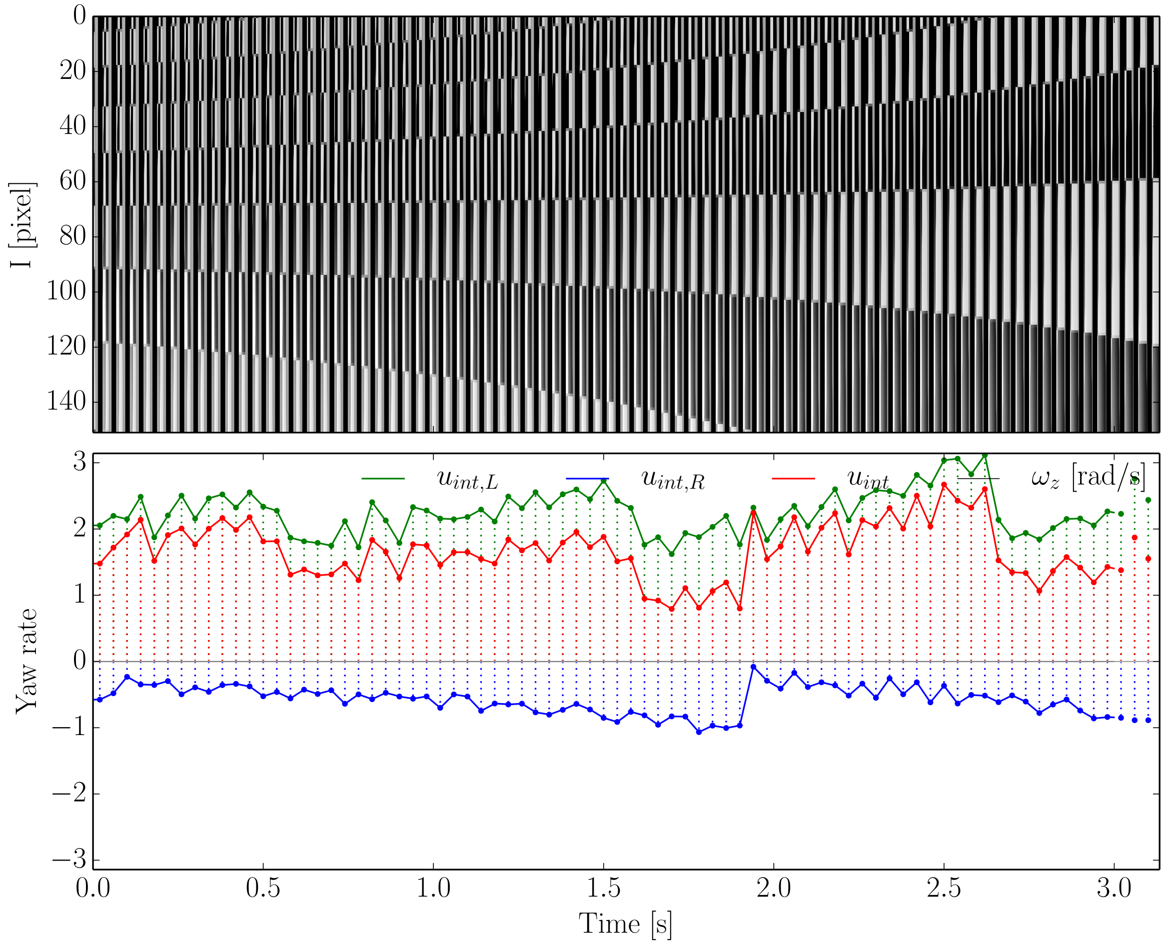

Figure 4.14: Looming simulation on a steady platform based on the experiment plotted in Figure 4.13 (please refer to that figure for a more detailed explanation of the signals plotted). Note that there's no oscillatory motion in this simulation, so the gyroscope signal is zero throughout).

4.6 Summary of results

Table 4.1 summarizes the results of the looming experiments on the VelociRoACH robot, while Table 4.2 does so for the camera dolly ones. It displays the mean and standard deviation of the yaw rotational rate as measured by the gyroscope and estimated by the optical flow algorithm, both before and after derotation. It also reports the optical flow output from a 3D smooth simulation of each of the experiments. Since not all experiments approached the wall at the same angle, we add a column for the average angle of approach, α, that is estimated from the OptiTrack ground truth position data.

As expected, the mean yaw rotational rate as reported by the gyroscope is very close to zero, while its standard deviation is larger for the VelociRoACH experiments. As observed in Section 4.5, looming experiments are expected to have a nonzero optical flow output mean, which is evident in most simulations and the non-derotated camera dolly experiments. Note

n	α [deg]	ω_z [rad/s]	u_{int}	$u_{int,derot}$	$u_{int,sim}$
1	-135.37	-0.08 ± 0.65	-0.09 ± 2.34	-0.05 ± 0.47	0.20 ± 0.40
2	-132.99	-0.05 ± 0.65	0.03 ± 2.14	-0.05 ± 0.69	0.48 ± 0.30
3	-141.94	-0.08 ± 0.67	-0.19 ± 2.07	-0.13 ± 0.55	-1.28 ± 0.31
4	-124.43	-0.07 ± 0.70	0.04 ± 2.47	-0.06 ± 0.39	1.94 ± 0.35
5	-133.14	-0.07 ± 0.53	0.16 ± 1.84	-0.07 ± 0.30	1.14 ± 0.45
6	-131.64	-0.09 ± 0.70	-0.31 ± 2.57	-0.05 ± 0.43	1.14 ± 0.44
7	-129.43	-0.09 ± 0.44	-0.10 ± 1.95	-0.06 ± 0.33	1.72 ± 0.49
8	-122.98	-0.06 ± 0.41	-0.06 ± 1.54	-0.08 ± 0.28	1.42 ± 0.40
9	-106.80	-0.08 ± 0.61	-0.18 ± 1.69	-0.03 ± 0.36	1.21 ± 0.32
10	-83.15	0.12 ± 1.01	0.29 ± 1.59	0.02 ± 0.17	-0.70 ± 0.31

Table 4.1: Looming experiment results before and after derotation on the VelociRoACH robot. We also report the results from a 3D smooth simulation matched to each of the individual experiments and the average angle of approach to the wall, α.

n	α [deg]	ω_z [rad/s]	u_{int}	$u_{int,derot}$	$u_{int,sim}$
1	-127.51	0.03 ± 0.02	0.65 ± 0.51	-0.09 ± 0.09	1.53 ± 0.42
2	-127.42	0.03 ± 0.01	0.72 ± 0.27	-0.03 ± 0.11	1.39 ± 0.52
3	-122.87	0.03 ± 0.01	0.94 ± 0.26	0.06 ± 0.10	1.68 ± 0.42
4	-113.58	0.04 ± 0.02	1.36 ± 0.88	-0.08 ± 0.35	1.47 ± 0.29
5	-113.86	0.04 ± 0.02	1.24 ± 0.75	-0.16 ± 0.74	1.33 ± 0.39
6	-103.97	0.04 ± 0.02	0.02 ± 0.71	-0.26 ± 0.40	0.72 ± 0.54
7	-82.98	0.03 ± 0.02	0.41 ± 0.83	-0.49 ± 0.41	-0.57 ± 0.44
8	-82.35	0.03 ± 0.02	0.46 ± 0.49	-0.20 ± 0.21	-0.69 ± 0.30
9	-81.90	0.03 ± 0.01	0.92 ± 0.47	-0.09 ± 0.19	-0.72 ± 0.41
10	-50.59	0.03 ± 0.01	0.61 ± 0.77	-0.50 ± 0.21	-0.41 ± 0.38

Table 4.2: Looming experiment results before and after derotation for the camera dolly. We also report on the results from a 3D smooth simulation matched to each of the individual experiments and the average angle of approach to the wall, α.

that some experiments and simulations are expected to give close to a zero looming output because they approached the checkerboard pattern almost perpendicularly. A negative sign signals that the angle of approach has crossed this perpendicular.

The VelociRoACH experiments show a relatively larger standard deviation for the yaw rotational signals due to the inherent unsteadiness of this legged platform. A portion of this unsteadiness seems to have been alleviated after derotation, as expressed by a reduced standard deviation, but we haven't quite recovered the looming checkerboard's information. In fact, for both types of experiments, derotation seems to consistently lower the standard deviation at the cost of the looming information when we analyze its average effect over the whole experiment. We'd instead like to recover an output similar to that of the smooth simulation, which includes the looming information while still having a relatively low standard deviation.

As previously mentioned, one of the limitations of the derotation algorithm is its reliance on interpolation of sub-pixel motions. The relatively low resolution of each image row (152 pixels) necessitates interpolation across the pixels' intensities when derotating by a portion of a pixel. This is better than having discrete jumps of intensity when the motion reaches an integer amount of pixels, but it also introduces some noise at the texture edges that is clearly observed in simulation, particularly as it affects the optical flow estimation of motion in perpendicular axes.

Another limitation of the algorithm is the conflicting information that exists on the camera pixels' field of view. Our best estimate for this value is $.005192\,\text{rad} \times .004765\,\text{rad}$, based on a derivation from the camera geometry as documented in its datasheet that has been confirmed through experimentation. Nonetheless, a small variation in either of these angles can represent a large hit in performance of the derotation algorithm.

Lastly, by observing Figure 3.3, one can see that, given that the board is a rigid body, the rotations around the gyroscope axes are the same as those around the camera axes. However, the rotations around the gyroscope's origin also represent translations of the camera, which, in turn, also imply shifts and rotations in the image frame of reference. The reason the algorithm does not account for these translations, which can be easily calculated given the board's geometry, is that their effect on the image frame is dependent on the distance to the objects that the camera is imaging, which cannot be known without extra sensors.

On top of all this, there is the non-negligible effect of gyroscope drift, which will accumulate on the integrated angle signals, causing us to overestimate the robot's motion and thus overcompensate for them.

4.7 Concluding remarks

We introduced image derotation to counteract the effects that an unsteady platform can have on optical flow estimation and analyzed its performance in experiments and simulations of robots approaching a checkerboard pattern.

The algorithm has not been able to counteract the unsteadiness introduced by the VelociRoACH's dynamics due to a number of limitations:

- Reliance on interpolation of sub-pixel motions,
- Conflicting information on the camera pixel's field of view,
- Not properly accounting for gyroscope drift,
- Not accounting for translations of the camera with respect to the gyroscope's center,
- The effect of the camera's rolling shutter
- The large motions of the robot produced motions beyond the EMD's estimation limits,

- Even comparisons to the simulation failed due to the hardship of properly reproducing the experiments (lighting, angle of approach, textures, contrast).

We achieve some minor improvements in the optical flow output when observing the algorithms' effect on a single row over a few frames. In particular, the resulting estimates lose the large amplitudes introduced by the robot's oscillations and even have reduced oscillatory energy (given the reduced standard deviation). On average, over a few rows, they recover at least partially the ability to recognize a looming wall when compared to the results on a steady platform.

When trying to apply the algorithm over a large set of frames and get the average optical flow result, though, we mostly see that the amplitude is smaller and the standard deviation is reduced, but the looming information has been lost. It is interesting to highlight that this also happens with the camera dolly experiments. Some of the algorithm's limitations, particularly gyroscope drift or a bad estimate for the pixel's field of view, might be partly to blame for these results.

Bibliography

Avadhanula, S., R. J. Wood, E. Steltz, J. Yan, and R. S. Fearing (2003). "Lift force improvements for the micromechanical flying insect". In: *IEEE/RSJ Int. Conf. on Intelligent Robots and Systems*. Las Vegas, NV, USA, pp. 1350–1356. DOI: 10.1109/IROS.2003.1248832.

Bachrach, A., R. He, and N. Roy (2009). "Autonomous Flight in Unknown Indoor Environments". In: *International Journal of Micro Air Vehicles* 1.4, pp. 217–228. DOI: 10.1260/175682909790291492.

Baek, S. S., F. L. Garcia Bermudez, and R. S. Fearing (2011). "Flight control for target seeking by 13 gram ornithopter". In: *IEEE/RSJ Int. Conf. on Intelligent Robots and Systems*, pp. 2674–2681. DOI: 10.1109/IROS.2011.6094581.

Baisch, A. T., C. Heimlich, M. Karpelson, and R. J. Wood (2011). "HAMR3: An autonomous 1.7g ambulatory robot". In: *2011 IEEE/RSJ International Conference on Intelligent Robots and Systems (IROS 2011)*. San Francisco, CA: IEEE, pp. 5073–5079. DOI: 10.1109/iros.2011.6095063.

Barrows, G. L., J. S. Chahl, and M. V. Srinivasan (2002). "Biomimetic Visual Sensing and Flight Control". In: *Proceedings of the 17th Bristol International UAV Systems Conference*. Bristol, UK.

Beyeler, A., J.-C. Zufferey, and D. Floreano (2007). "3D Vision-based Navigation for Indoor Microflyers". In: *Robotics and Automation, 2007 IEEE International Conference on*. IEEE. Roma, Italy, pp. 1336–1341. DOI: 10.1109/ROBOT.2007.363170.

Birkmeyer, P., A. G. Gillies, and R. S. Fearing (2011). "CLASH: Climbing vertical loose cloth". In: *IEEE/RSJ Int. Conf. on Intelligent Robots and Systems*, pp. 5087–5093. DOI: 10.1109/IROS.2011.6094905.

Birkmeyer, P., K. Peterson, and R. S. Fearing (2009). "DASH: A dynamic 16g hexapedal robot". In: *IEEE/RSJ Int. Conf. on Intelligent Robots and Systems*, pp. 2683–2689. DOI: 10.1109/IROS.2009.5354561.

Borst, A. (2007). "Correlation versus gradient type motion detectors: the pros and cons". In: *Phil. Trans. R. Soc. B* 362.1479, pp. 369–374. DOI: 10.1098/rstb.2006.1964.

Brinkworth, R. S. A. and D. C. O'Carroll (2009). "Robust Models for Optic Flow Coding in Natural Scenes Inspired by Insect Biology". In: *PLoS Comput Biol* 5.11, e1000555. DOI: 10.1371/journal.pcbi.1000555.

Cham, J. G., J. K. Karpick, and M. R. Cutkosky (2004). "Stride Period Adaptation of a Biomimetic Running Hexapod". In: *The International Journal of Robotics Research* 23.2, pp. 141–153. DOI: 10.1177/0278364904041323.

Clark, J. E. and M. R. Cutkosky (2006). "The Effect of Leg Specialization in a Biomimetic Hexapedal Running Robot". In: *Journal of Dynamic Systems, Measurement, and Control* 128.1, pp. 26+. DOI: 10.1115/1.2168477.

Conroy, J., G. Gremillion, B. Ranganathan, and J. S. Humbert (2009). "Implementation of wide-field integration of optic flow for autonomous quadrotor navigation". In: *Autonomous Robots* 27.3, pp. 189–198.

de Croon, G. C. H. E., E. de Weerdt, C. de Wagter, and B. D. W. Remes (2010). "The appearance variation cue for obstacle avoidance". In: Tianjin, China, pp. 1606–1611. DOI: 10.1109/ROBIO.2010.5723570.

Dickinson, M. H., F.-O. Lehmann, and S. P. Sane (1999). "Wing Rotation and the Aerodynamic Basis of Insect Flight". In: *Science* 284.5422, pp. 1954–1960.

Duhamel, P. E. J., N. O. Perez-Arancibia, G. L. Barrows, and R. J. Wood (2012). "Altitude feedback control of a flapping-wing microrobot using an on-board biologically inspired optical flow sensor". In: *Robotics and Automation (ICRA), 2012 IEEE International Conference on*. IEEE, pp. 4228–4235. DOI: 10.1109/ICRA.2012.6225313.

Egelhaaf, M. and W. Reichardt (1987). "Dynamic response properties of movement detectors: Theoretical analysis and electrophysiological investigation in the visual system of the fly". In: *Biological Cybernetics* 56.2, pp. 69–87. DOI: 10.1007/BF00317982.

Espenschied, K., R. Quinn, R. Beer, and H. Chiel (1996). "Biologically based distributed control and local reflexes improve rough terrain locomotion in a hexapod robot". In: *Robotics and Autonomous Systems* 18.1-2, pp. 59–64. DOI: 10.1016/0921-8890(96)00003-6.

Expert, F. and F. Ruffier (2012). "Controlling docking, altitude and speed in a circular high-roofed tunnel thanks to the optic flow". In: *2012 IEEE/RSJ International Conference on Intelligent Robots and Systems (IROS 2012)*. Vilamoura-Algarve, Portugal: IEEE, pp. 1125–1132. DOI: 10.1109/iros.2012.6385946.

Ferris, D. P., M. Louie, and C. T. Farley (1998). "Running in the real world: adjusting leg stiffness for different surfaces". In: *Proceedings of the Royal Society of London. Series B: Biological Sciences* 265.1400, pp. 989–994. DOI: 10.1098/rspb.1998.0388.

Franceschini, N., A. Riehle, and A. Le Nestour (1989). "Directionally selective motion detection by insect neurons". In: *Facets of vision*. Ed. by D. G. Stavenga and R. Hardie. Berlin and New York: Springer, pp. 360–390.

Galloway, K. C., J. E. Clark, M. Yim, and D. E. Koditschek (2011). "Experimental Investigations into the Role of Passive Variable Compliant Legs for Dynamic Robotic Locomotion". In: *IEEE/RSJ Int. Conf. on Robotics and Automation*. Shanghai, China.

Garcia Bermudez, F. L. and R. S. Fearing (2009). "Optical Flow on a Flapping Wing Robot". In: *Intelligent Robots and Systems, 2009. IROS 2009. IEEE/RSJ International Conference on*. St. Louis, MO, USA, pp. 5027–5032. DOI: 10.1109/IROS.2009.5354337.

Garcia Bermudez, F. L., R. C. Julian, D. W. Haldane, P. Abbeel, and R. S. Fearing (2012). "Performance analysis and terrain classification for a legged robot over rough terrain". In: *2012 IEEE/RSJ International Conference on Intelligent Robots and Systems (IROS 2012)*. Vilamoura-Algarve, Portugal: IEEE, pp. 513–519. DOI: 10.1109/IROS.2012.6386243.

Haag, J., W. Denk, and A. Borst (2004). "Fly motion vision is based on Reichardt detectors regardless of the signal-to-noise ratio". In: *Proceedings of the National Academy of Sciences of the United States of America* 101.46, pp. 16333–16338. DOI: 10.1073/pnas.0407368101.

Haldane, D. W., K. C. Peterson, F. L. Garcia Bermudez, and R. S. Fearing (2013). "Animal-inspired design and aerodynamic stabilization of a hexapedal millirobot". In: *2013 IEEE International Conference on Robotics and Automation (ICRA)*. Karlsruhe, Germany: IEEE, pp. 3279–3286. DOI: 10.1109/icra.2013.6631034.

Hassenstein, V. B. and W. Reichardt (1956). "Systemtheoretische Analyse der Zeit-, Reihenfolgen- und Vorseichenauswertung bei der Berwegungsperzeption des Rüsselkäfers *Chlorophanus*". In: *Zeitschrift für Naturforschung B* 11.9, pp. 513–524.

Herisse, B., S. Oustrieres, T. Hamel, R. Mahony, and F.-X. Russotto (2010). "A general optical flow based terrain-following strategy for a VTOL UAV using multiple views". In: *Robotics and Automation, 2010. ICRA 2010. IEEE International Conference on.* Anchorage, Alaska. DOI: 10.1109/ROBOT.2010.5509536.

Hoffman, K. L. and R. J. Wood (2011). "Passive undulatory gaits enhance walking in a myriapod millirobot". In: *2011 IEEE/RSJ International Conference on Intelligent Robots and Systems (IROS 2011)*. San Francisco, CA: IEEE, pp. 1479–1486. DOI: 10.1109/iros.2011.6094700.

Hoover, A. M., S. Burden, X.-Y. Fu, S. Shankar Sastry, and R. S. Fearing (2010). "Bio-inspired design and dynamic maneuverability of a minimally actuated six-legged robot". In: *IEEE RAS/EMBS Int. Conf. on Biomedical Robotics and Biomechatronics*. Tokyo, Japan, pp. 869–876. DOI: 10.1109/BIOROB.2010.5626034.

Hoover, A. M. and R. S. Fearing (2008). "Fast scale prototyping for folded millirobots". In: *2008 IEEE International Conference on Robotics and Automation (ICRA)*. Pasadena, CA, USA: IEEE, pp. 886–892. DOI: 10.1109/robot.2008.4543317.

Hoover, A. M., E. E. Steltz, and R. S. Fearing (2008). "RoACH: An autonomous 2.4g crawling hexapod robot". In: *IEEE Int. Conf. on Intelligent Robots and Systems*. Nice, France, pp. 26–33.

Huston, S. J. and H. G. Krapp (2008). "Visuomotor Transformation in the Fly Gaze Stabilization System". In: *PLoS Biology* 6.7, pp. 1468–1478. DOI: 10.1371/journal.pbio.0060173.

Iida, F. (2003). "Biologically inspired visual odometer for navigation of a flying robot". In: *Robotics and Autonomous Systems* 44.3-4, pp. 201–208.

Joesch, M., F. Weber, H. Eichner, and A. Borst (2013). "Functional Specialization of Parallel Motion Detection Circuits in the Fly". In: *Journal of Neuroscience* 33.3, pp. 902–905. DOI: 10.1523/jneurosci.3374-12.2013.

Kerhuel, L., S. Viollet, and N. Franceschini (2010). "Steering by Gazing: An Efficient Biomimetic Control Strategy for Visually Guided Micro Aerial Vehicles". In: *Robotics, IEEE Transactions on* 26.2, pp. 307–319. DOI: 10.1109/TRO.2010.2042537.

Kohut, N. J., A. M. Hoover, K. Y. Ma, S. S. Baek, and R. S. Fearing (2011). "MEDIC: A legged millirobot utilizing novel obstacle traversal". In: *IEEE Int. Conf. on Robotics and Automation*, pp. 802–808. DOI: 10.1109/ICRA.2011.5980360.

Kohut, N., A. Pullin, D. W. Haldane, D. Zarrouk, and R. S. Fearing (2013). "Precise dynamic turning of a 10 cm legged robot on a low friction surface using a tail". In: *2013 IEEE International Conference on Robotics and Automation (ICRA)*. Karlsruhe, Germany: IEEE, pp. 3299–3306. DOI: 10.1109/icra.2013.6631037.

Kolter, J. Z., M. P. Rodgers, and A. Y. Ng (2008). "A control architecture for quadruped locomotion over rough terrain". In: *IEEE Int. Conf. on Robotics and Automation*, pp. 811–818. DOI: 10.1109/ROBOT.2008.4543305.

Land, M. F. (1997). "Visual Acuity in Insects". In: *Annual Review of Entomology* 42, pp. 147–177. DOI: 10.1146/annurev.ento.42.1.147.

Lentink, D., S. R. Jongerius, and N. L. Bradshaw (2010). "The Scalable Design of Flapping Micro-Air Vehicles Inspired by Insect Flight". In: *Flying Insects and Robots*. Ed. by D. Floreano, J.-C. Zufferey, M. V. Srinivasan, and C. Ellington. Berlin, Heidelberg: Springer Berlin Heidelberg. Chap. 14, pp. 185–205. DOI: 10.1007/978-3-540-89393-6_14.

Li, C., A. M. Hoover, P. Birkmeyer, P. B. Umbanhowar, R. S. Fearing, and D. I. Goldman (2010). "Systematic study of the performance of small robots on controlled laboratory substrates". In: *SPIE Conf. on Micro- and Nanotechnology Sensors, Systems, and Applications*. Orlando, Florida, USA, pages. DOI: 10.1117/12.851047.

Li, C., P. B. Umbanhowar, H. Komsuoglu, D. E. Koditschek, and D. I. Goldman (2009). "Sensitive dependence of the motion of a legged robot on granular media". In: *Proceedings of the National Academy of Sciences*. DOI: 10.1073/pnas.0809095106.

Ma, K. Y., P. Chirarattananon, S. B. Fuller, and R. J. Wood (2013). "Controlled Flight of a Biologically Inspired, Insect-Scale Robot". In: *Science* 340.6132, pp. 603–607. DOI: 10.1126/science.1231806.

Maisak, M. S., J. Haag, G. Ammer, E. Serbe, M. Meier, A. Leonhardt, T. Schilling, A. Bahl, G. M. Rubin, A. Nern, B. J. Dickson, D. F. Reiff, E. Hopp, and A. Borst (2013). "A directional tuning map of Drosophila elementary motion detectors". In: *Nature* 500.7461, pp. 212–216. DOI: 10.1038/nature12320.

Moore, R. J. D., S. Thurrowgood, and M. V. Srinivasan (2012). "Vision-only estimation of wind field strength and direction from an aerial platform". In: *2012 IEEE/RSJ International Conference on Intelligent Robots and Systems (IROS 2012)*. Vilamoura-Algarve, Portugal: IEEE, pp. 4544–4549. DOI: 10.1109/iros.2012.6385682.

Peters, J. and S. Schaal (2006). "Policy Gradient Methods for Robotics". In: *IEEE/RSJ Int. Conf. on Intelligent Robots and Systems*. Beijing, China, pp. 2219–2225. DOI: 10.1109/IROS.2006.282564.

Peterson, K., P. Birkmeyer, R. Dudley, and R. S. Fearing (2011). "A wing-assisted running robot and implications for avian flight evolution". In: *Bioinspiration & Biomimetics* 6.4, pp. 046008+. DOI: 10.1088/1748-3182/6/4/046008.

Peterson, K. and R. S. Fearing (2011). "Experimental dynamics of wing assisted running for a bipedal ornithopter". In: *2011 IEEE/RSJ International Conference on Intelligent Robots and Systems (IROS 2011)*. San Francisco, CA: IEEE, pp. 5080–5086. DOI: 10.1109/iros.2011.6095041.

Plett, J., A. Bahl, M. Buss, K. Kühnlenz, and A. Borst (2012). "Bio-inspired visual ego-rotation sensor for MAVs". In: *Biological Cybernetics*, pp. 1–13. DOI: 10.1007/s00422-012-0478-6.

Pullin, A. O., N. J. Kohut, D. Zarrouk, and R. S. Fearing (2012). "Dynamic turning of 13 cm robot comparing tail and differential drive". In: *IEEE Int. Conf. on Robotics and Automation*.

Qian, F., T. Zhang, C. Li, P. Masarati, A. M. Hoover, P. Birkmeyer, A. Pullin, R. S. Fearing, and D. I. Goldman (2012). "Walking and running on yielding and fluidizing ground". In: *Robotics: Science and Systems*. Sidney, Australia.

Reichardt, W. (1961). "Autocorrelation, a principle for the evaluation of sensory information by the central nervous system". In: *Principles of Sensory Communication*. Ed. by W. Rosenblith. New York: Wiley, pp. 303–317.

— (1987). "Evaluation of optical motion information by movement detectors". In: *Journal of Comparative Physiology A: Neuroethology, Sensory, Neural, and Behavioral Physiology* 161.4, pp. 533–547. DOI: 10.1007/BF00603660.

Reiser, M. B. and M. H. Dickinson (2003). "A test bed for insect-inspired robotic control". In: *Philosophical Transactions: Mathematical, Physical and Engineering Sciences* 361.1811, pp. 2267–2285.

Ruffier, F. and N. Franceschini (2005). "Optic flow regulation: the key to aircraft automatic guidance". In: *Robotics and Autonomous Systems* 50.4, pp. 177–194.

Saranli, U., M. Buehler, and D. E. Koditschek (2001). "RHex: A Simple and Highly Mobile Hexapod Robot". In: *The International Journal of Robotics Research* 20.7, pp. 616–631. DOI: 10.1177/02783640122067570.

Seipel, J. and P. Holmes (2007). "A simple model for clock-actuated legged locomotion". In: *Regular and Chaotic Dynamics* 12.5, pp. 502–520. DOI: 10.1134/S1560354707050048.

Single, S. and A. Borst (1998). "Dendritic Integration and Its Role in Computing Image Velocity". In: *Science* 281.5384, pp. 1848–1850.

Srinivasan, M. V., S. Zhang, J. Chahl, G. Stange, and M. Garrat (2004). "An overview of insect-inspired guidance for application in ground and airborne platforms". In: *Proceedings of the Institution of Mechanical Engineers, Part G: Journal of Aerospace Engineering* 218.6, pp. 375–388. DOI: 10.1243/0954410042794966.

van Hateren, J. and C. Schilstra (1999). "Blowfly flight and optic flow. II. Head movements during flight". In: *J Exp Biol* 202.11, pp. 1491–1500.

Weingarten, J. D., G. A. D. Lopes, M. Buehler, R. E. Groff, and D. E. Koditschek (2004). "Automated gait adaptation for legged robots". In: *IEEE Int. Conf. on Robotics and Automation*. Vol. 3, 2153–2158 Vol.3. DOI: 10.1109/ROBOT.2004.1307381.

Wood, R. J. (2008). "The First Takeoff of a Biologically Inspired At-Scale Robotic Insect". In: *IEEE Transactions on Robotics* 24.2, pp. 341–347. DOI: 10.1109/TRO.2008.916997.

Wood, R., S. Avadhanula, E. Steltz, M. Seeman, J. Entwistle, A. Bachrach, G. Barrows, S. Sanders, and R. Fearing (2005). "Design, fabrication and initial results of a 2g autonomous glider". In: *Industrial Electronics Society Conference (IECON)*. IEEE. DOI: 10.1109/IECON.2005.1569190.

Zarrouk, D., A. Pullin, N. Kohut, and R. S. Fearing (2013). "STAR, a sprawl tuned autonomous robot". In: *2013 IEEE International Conference on Robotics and Automation (ICRA)*. Karlsruhe, Germany: IEEE, pp. 20–25. DOI: 10.1109/icra.2013.6630551.

Zingg, S., D. Scaramuzza, S. Weiss, and R. Siegwart (2010). "MAV navigation through indoor corridors using optical flow". In: *Robotics and Automation, 2010. ICRA 2010. IEEE International Conference on*. Anchorage, AK, pp. 3361–3368. DOI: 10.1109/ROBOT.2010.5509777.

Zufferey, J.-C., A. Beyeler, and D. Floreano (2010). "Autonomous flight at low altitude with vision-based collision avoidance and GPS-based path following". In: *Robotics and Automation, 2010. ICRA 2010. IEEE International Conference on*. Anchorage, Alaska.

Zufferey, J.-C. and D. Floreano (2006). "Fly-inspired visual steering of an ultralight indoor aircraft". In: *IEEE Transactions on Robotics* 22.1, pp. 137–146.

Zufferey, J.-C., A. Guanella, A. Beyeler, and D. Floreano (2006). "Flying over the reality gap: From simulated to real indoor airships". In: *Autonomous Robots* 21.3, pp. 243–254. DOI: 10.1007/s10514-006-9718-8.